Exploratory High-Resolution Climate Simulations using the Community Atmosphere Model (CAM)

JULIO T. BACMEISTER

Atmospheric Modeling and Prediction Section, National Center for Atmospheric Research, Boulder, Colorado*

MICHAEL F. WEHNER

Lawrence Berkeley National Laboratory, Berkeley, California

RICHARD B. NEALE, ANDREW GETTELMAN, CECILE HANNAY, PETER H. LAURITZEN, JULIE M. CARON, AND JOHN E. TRUESDALE

Atmospheric Modeling and Prediction Section, National Center for Atmospheric Research, Boulder, Colorado*

(Manuscript received 27 June 2013, in final form 21 November 2013)

ABSTRACT

Extended, high-resolution (0.23° latitude × 0.31° longitude) simulations with Community Atmosphere Model versions 4 and 5 (CAM4 and CAM5) are examined and compared with results from climate simulations conducted at a more typical resolution of 0.9° latitude × 1.25° longitude. Overall, the simulated climate of the high-resolution experiments is not dramatically better than that of their low-resolution counterparts. Improvements appear primarily where topographic effects may be playing a role, including a substantially improved summertime Indian monsoon simulation in CAM4 at high resolution. Significant sensitivity to resolution is found in simulated precipitation over the southeast United States during winter. Some aspects of the simulated seasonal mean precipitation deteriorate notably at high resolution. Prominent among these is an exacerbated Pacific "double ITCZ" bias in both models. Nevertheless, while large-scale seasonal means are not dramatically better at high resolution, realistic tropical cyclone (TC) distributions are obtained. Some skill in reproducing interannual variability in TC statistics also appears.

1. Introduction

Thanks to the development of highly scalable dynamical cores (e.g., Putman et al. 2005; Satoh et al. 2008; Dennis et al. 2012) that can exploit massively parallel computer architectures, we expect that global climate models in the next decade will run routinely at horizontal resolutions of 25 km or finer. Early results from climate simulations at these resolutions are promising in some respects. The models begin to explicitly capture important mesoscale convective phenomena such as tropical cyclones (Zhao et al. 2009; Manganello et al. 2012). Statistics for midlatitude cyclones and blocking events are also improved at resolutions near 25 km (Jung et al. 2012) along with the representation of orographically induced and coastal sea-breeze circulations (Boyle and Klein 2010). Nevertheless, climate simulations at horizontal resolutions of 25 km or finer are still a significant computational burden even at dedicated centers such as the National Center for Atmospheric Research (NCAR). Furthermore, as will be seen below, early results at these resolutions, while encouraging in their improved representation of some orographic and mesoscale circulations, do not yield dramatic improvements in many important aspects of model climatology. In fact, some biases such as excessive precipitation in the ITCZs are actually seen to get worse at high resolution.

*The National Center for Atmospheric Research is sponsored by the National Science Foundation.

Corresponding author address: Julio T. Bacmeister, Atmospheric Modeling and Prediction Section, NCAR, Boulder, CO 80301.
E-mail: juliob@ucar.edu

DOI: 10.1175/JCLI-D-13-00387.1

Optimizing choices for empirical parameters in physical parameterizations (i.e., "tuning") at high resolution is difficult, and assumptions made in formulating many physical parameterizations break down as resolution approaches 10 km. In this paper we describe early efforts to characterize Community Atmosphere Model (CAM) behavior at high horizontal resolutions. Our high-resolution simulations were performed with only few changes to CAM's physical parameterization schemes as they are implemented for typical climate resolutions of 100 km. The intent of this paper is to highlight the salient initial successes and shortcomings of CAM runs at high resolutions (for climate studies) of 25 km.

The paper is organized as follows. Section 2 describes the model configurations, experimental setups, and verification data used in this study. Modifications made to the model configurations for high-resolution runs are explained. Section 3 examines top-of-the-atmosphere radiation fluxes and their sensitivities to resolution. Section 4 discusses basic model climatologies of several key simulation parameters, including upper-level winds, surface pressure, and precipitation. Precipitation intensity distributions and partitioning between convective and large-scale sources are also shown. Section 5 briefly describes simulated intraseasonal variability in the tropics. Section 6 focuses on regional aspects of the simulated precipitation over the United States. Resolution is shown to have different impacts in winter and summer seasons. Section 7 discusses tropical cyclone climatology in the high-resolution simulations. Finally, in section 8 key results are summarized.

2. Models, experimental design, and verification data

We will analyze results from CAM forced by observed sea surface temperature (SST) data. The bulk of our results come from four simulations that were initialized on 1 January 1979 and integrated for at least 25 simulation years. A small amount of testing was performed utilizing shorter runs from 12 to 18 months, also forced by observed SSTs. Monthly-mean SST data on a $1^\circ \times 1^\circ$ grid are obtained according to the procedure in Hurrell et al. (2008). Monthly mean SSTs are assumed to be valid at the midpoint of each month. For other days, SSTs are obtained by linearly interpolating means for the current month and the preceding or following month depending on whether the current time falls before or after the midpoint of the month. A correction is applied to ensure that the accumulated means of the daily SSTs obtained this way are equal to the original monthly means (Taylor et al. 2000). Coupling software calculates air–sea fluxes and conservatively maps to the atmospheric model grid.

All simulations here use the CAM finite-volume dynamical core (CAM-FV; Lin 2004) on a latitude–longitude grid at two resolutions: 0.9° latitude × 1.25° longitude (0.9 × 1.25 henceforth) and 0.23° latitude × 0.31° longitude (0.23 × 0.31 henceforth). We use two versions (versions 4 and 5) of CAM model physics—CAM4 and CAM5 (Neale et al. 2010, 2012). Our 0.23 × 0.31 simulations include a new formulation of enhanced momentum dissipation near the model top (Lauritzen et al. 2012b), which is included for stability.

An extensive suite of monthly-mean diagnostics was saved for all model runs (see http://www.cgd.ucar.edu/amp/amwg/diagnostics/). In addition, 3-hourly averages of precipitation and radiative fluxes were saved for all runs. Instantaneous surface pressure, sea level pressure, near-surface winds, and precipitation were also saved every 3 h for the high-resolution runs. Our CAM5 high-resolution simulation also saved instantaneous winds and temperatures at 850 and 200 hPa and temperatures at 500 hPa every 3 h in order to enable a variety of tropical cyclone algorithms to be employed (see the appendix).

a. *CAM4 versus CAM5*

CAM4 physics have been described in detail by Neale et al. (2010). A key innovation in CAM4 was the introduction of an entraining test plume, as well as a parameterization of cumulus momentum transport into the model's deep convection scheme (Zhang and McFarlane 1995; Neale et al. 2008). These changes led to improved El Niño–Southern Oscillation variability in coupled simulations (Neale et al. 2008).

The differences in physics between CAM4 to CAM5 are extensive and involve every major physics parameterization except for deep convection, which remained as in CAM4 (Neale et al. 2012). An important development in CAM5 is an improved two-moment representation of cloud microphysical processes that is directly coupled to aerosol mass and number concentrations. Initial liquid cloud fraction is based on a threshold relative humidity as well as mass detrainment from both shallow and deep convection. Ice microphysics are treated prognostically (Morrison and Gettelman 2008; Gettelman et al. 2010). Cloud fractions are then adjusted via an iterative algorithm (Park et al. 2014, manuscript submitted to *J. Climate*) that ensures consistency between fractions and condensates. CAM4 uses simpler microphysics and macrophysics based on critical relative humidity thresholds (Rasch and Kristjansson 1998).

Both of our 0.23 × 0.31, 25-yr simulations incorporated some modifications to the default model physics used at 0.9 × 1.25. In the case of CAM4 these modifications were aimed at improving top-of-the-atmosphere (TOA) radiation fluxes, while in CAM5 the modifications

were aimed at eliminating the computational cost incurred by using prognostic aerosols. We evaluated these modifications by comparing against short (1 yr) simulations at 0.23 × 0.31 using the default CAM4 and CAM5 configurations.

1) Prescribed bulk aerosols for high-resolution CAM5

CAM5 physics include a sophisticated three-moment modal aerosol model (MAM; Easter et al. 2004; Ghan and Easter 2006). This treatment requires the inclusion of 20 new, fully prognostic aerosol quantities. The computational cost per grid point time step of CAM5 with fully prognostic aerosols is approximately 5 times that of CAM4. For an exploratory forced SST run at high resolution the costs of including fully prognostic aerosols were expected to outweigh the scientific benefits. To reduce computational cost we implemented a simple prescribed aerosol configuration based on an earlier bulk aerosol model (BAM; Kiehl et al. 2000). Monthly mean bulk aerosol masses from CAM4 simulations are used as input. A prescribed aerosol mass–number relationship is used to determine aerosol numbers. These prescribed aerosol masses and numbers are then used as input to the model's cloud microphysics scheme exactly as is done when the prognostic aerosol model is used. Cloud radiative forcing was tuned for agreement with the fully prognostic MAM aerosol configuration by adjusting the prescribed aerosol mass–number relationship for sulfate. This tuning was performed at 0.9 × 1.25 and carried over to 0.23 × 0.31 with no modification.

This "prescribed BAM" configuration reduces the cost of running CAM5 by a factor of 2. Comparisons of this configuration with a 1-yr integration using fully prognostic MAM aerosols at 0.23 × 0.31 are shown in section 3. As will be shown, the use of the prescribed BAM versus the prognostic MAM configuration has only small effects on top-of-the-atmosphere radiative fluxes.

2) Ice-cloud modifications for high-resolution CAM4

Early attempts to use CAM4 at 0.23 × 0.31 resolution in coupled simulations revealed undesirable changes in cloud radiative forcing. Longwave cloud forcing (LWCF) and shortwave cloud wave forcing (SWCF) at mid and high latitudes were seen to decrease dramatically at high horizontal resolution. We believe these cloud forcing biases could contribute to unrealistic Northern Hemisphere sea ice distributions and large mid- and high-latitude SST biases (e.g., Kirtman et al. 2013). While further high-resolution coupled simulations with CAM4 may take place, further development of CAM4 physics is not planned at NCAR. To provide an alternative CAM4 configuration for high resolution, we tested a number of tuning parameter changes and minimal code changes in an effort to reduce LWCF and SWCF biases at mid and high latitudes.

A very satisfactory result was obtained by changing the dependence of effective ice-cloud radius on temperature. In the standard CAM4 implementation ice-cloud effective radii become very large (>100 μm) as temperatures approach 273 K (Kristjánsson et al. 2000). This results in high fall speeds and rapid loss of both mass and fraction due to sedimentation, as well as producing low optical depths for any remaining "warm" ice cloud. We modified the dependence of ice-cloud radii on temperature T to follow

$$r_{\text{eff}} = \begin{cases} 25, & T < 224\,\text{K} \\ 25 + \dfrac{15}{50}(224 - T), & 224 \le T < 274\,\text{K}\,, \\ 10, & T \ge 274\,\text{K} \end{cases} \tag{1}$$

where r_{eff} is given in microns. We have no observational basis for the radius dependence in Eq. (1); however, one possible cause of reduced effective particle radii at temperatures near freezing is the presence of mixed phase clouds, which may be underrepresented in CAM4 (Storelvmo et al. 2008). Changes in ice-particle habits (Turner 2005), as well as the presence of liquid droplets, may also result in smaller effective particle radii for mixed phase clouds. The primary intent of the modification in Eq. (1) is to reproduce the 0.9 × 1.25 TOA radiative fluxes at 0.23 × 0.31 resolution in order to minimize impacts on future coupled simulations. As will be seen section 3, this has been largely accomplished.

b. *Verification data*

Simulated radiative fluxes are compared with gridded monthly means from Clouds and the Earth's Radiant Energy System–Energy Balanced and Filled (CERES-EBAF; Loeb et al. 2009) datasets. We also examine simulated winds, sea level pressure, moisture fields, and surface precipitation fluxes. Gridded reanalysis data from ERA-Interim (Dee et al. 2011) are used to verify winds, moisture profiles, and sea level pressure fields. Observational estimates of precipitation are obtained from the Global Precipitation Climatology Project (GPCP; Huffman et al. 1997; Xie et al. 2003) and the combined-sensor product of the Tropical Rainfall Measuring Mission (TRMM 3B42; Huffman et al. 2007). Estimates of total precipitable water are obtained from the National Aeronautics and Space Administration (NASA) Water Vapor Project (NVAP; Randel et al. 1996).

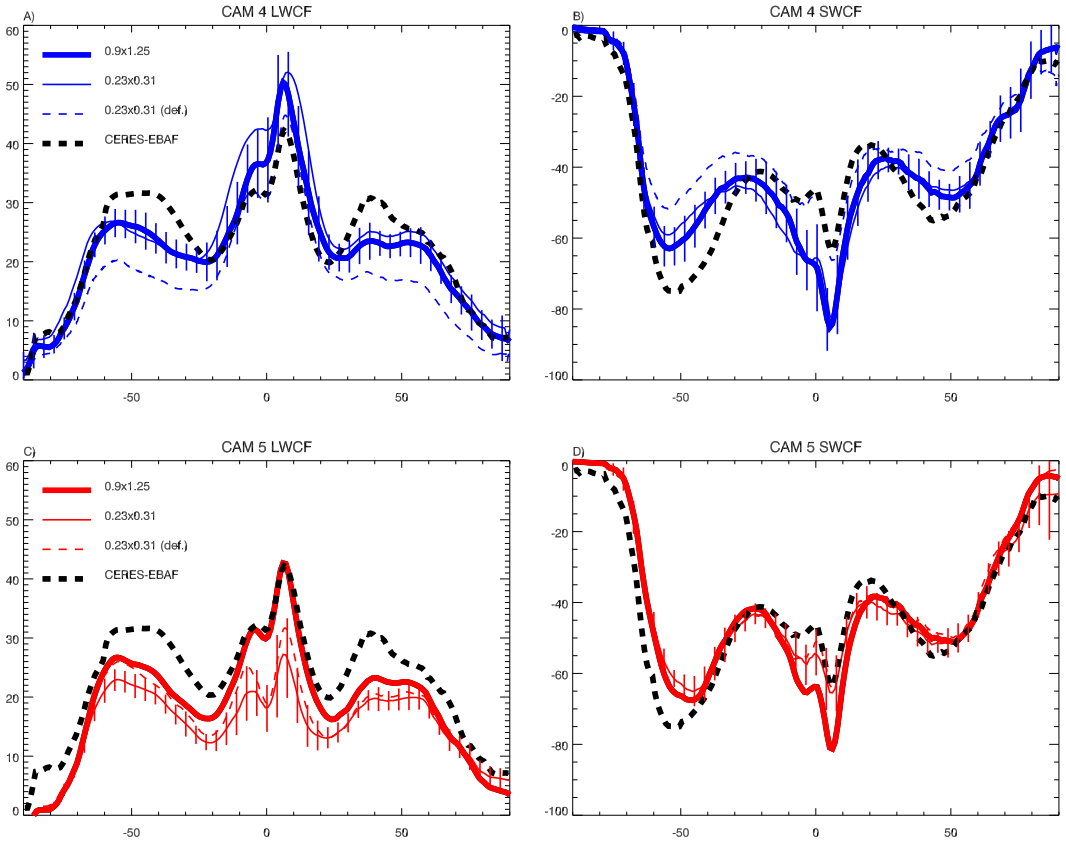

FIG. 1. Annual mean, zonally averaged (left) LWCF and (right) SWCF as a function of latitude. In each panel, the black, dashed lines show CERES-EBAF estimates of each flux. (a),(b) Blue lines show results for CAM4. Thick lines show the 25-yr, 1980–2004 annual means for the CAM4 0.9 × 1.25 AMIP run, with vertical lines indicating standard deviations. The thin dashed lines show results from a single year of a 0.23 × 0.31 run using default CAM4 physics. The thin solid blue lines show 25-yr annual means from the CAM4 0.23 × 0.31 run the using modified ice cloud radii discussed in section 2. (c),(d) Red lines show CAM5 results. Thick lines show 25-yr means for CAM5 0.9 × 1.25. Thin solid lines show 25-yr means for CAM5 0.23 × 0.31 using prescribed BAM aerosols. The thin dashed lines show means for a single year using the full CAM5 aerosol model at 0.23 × 0.31.

3. Top-of-the-atmosphere radiation balance

Zonal and global means

Figures 1a and 1b show zonally averaged, annual mean LWCF and SWCF in CAM4. Thick blue lines show mean annual-average fluxes for 1980–2004 in the CAM4 0.9 × 1.25 run. The vertical blue lines show the root-mean-square (RMS) deviations over the period. Dashed blue lines show fluxes from a single year in a run using 0.23 × 0.31 resolution with default CAM4 physics. The impact of resolution on cloud forcing is obvious. Large, relatively uniform 5–10 W m^{-2} reductions in both LWCF and SWCF are found poleward of 25° in both hemispheres. This is accompanied by large decreases in high and middle cloud fractions (not shown).

The thin solid blue lines in Figs. 1a and 1b show the 1980–2004 annually and zonally averaged LWCF and SWCF from CAM4 0.23 × 0.31 using the modified ice particle sizes in Eq. (1). The modified relationship between r_{eff} and T results in significantly increased cloud-radiative forcing at 0.23 × 0.31. Annual means of both LWCF and SWCF in the high-resolution CAM4 run are now within the RMS variations from the 0.9 × 1.25 run at most latitudes. Observational estimates of LWCF or SWCF from CERES-EBAF are shown by the thick black dashed lines in each panel. The 0.9 × 1.25 results, as well as those from the 0.23 × 0.31 run with modified ice clouds, are clearly closer to CERES-EBAF than the default 0.23 × 0.31 results.

Table 1 gives mean annually and globally averaged radiation fluxes for 1980–2004 from our simulations compared with estimates from CERES-EBAF. The three columns on the right show results for CAM4. Fluxes in CAM4 0.23 × 0.31 with modified ice are close to those in CAM4 0.9 × 1.25. An increase in the top-of-model (TOM) residual has occurred, from 1 W m^{-2} at

TABLE 1. Annually averaged, global mean radiation fluxes ($W m^{-2}$) in CAM.

		CAM5		CAM4		
	CERES	0.23 × 0.31	0.9 × 1.25	0.23 × 0.31	0.9 × 1.25	0.23 × 0.31 (def.)
Residual (TOM)	—	−3.3	0.67	2.1	1.02	2.7
Net longwave (TOM)	—	242.5	236.7	236.5	238.0	242.7
Net shortwave (TOM)	—	239.2	237.4	238.6	239.0	245.5
LWCF	26.5	17.2	22.3	28.3	25.7	21.1
SWCF	−47.1	−46.8	−48.5	−48.9	−48.1	−43.0
Clear-sky longwave (TOA)	266.5	261.1	260.4	265.9	264.8	264.9
Clear-sky shortwave (TOA)	287.6	289.5	289.3	290.5	290.2	291.5

0.9 × 1.25 to 2.1 $W m^{-2}$ at 0.23 × 0.31, but individual longwave and shortwave fluxes remain similar, and are close to the CERES-EBAF estimates. The TOM residual in CAM4 0.23 × 0.31 (def.) is only slightly larger than in CAM4 0.23 × 0.31, but masks larger compensating biases in longwave and shortwave fluxes. We note that the high-resolution simulations presented here are too far out of radiative balance for use in coupled simulations. However, imbalances of a few watts per square meter in CAM can typically be addressed by small modifications to cloud fraction parameters that have little impact on other aspects of the simulations.

Figures 1c and 1d show annually and zonally averaged LWCF and SWCF from CAM5. Thick red lines show the 1980–2004 annually averaged zonal means from CAM5 0.9 × 1.25 with fully prognostic aerosols. Fluxes from a single year of CAM5 0.23 × 0.31 using the default fully prognostic aerosols are shown by the dashed thin red lines, while the solid thin red lines show the 1980–2004 means for CAM5 0.23 × 0.31 with prescribed BAM aerosol. The impact of replacing the default fully prognostic MAM model with the more economical prescribed BAM is generally small and well within the RMS deviations for 1980–2004 from the prescribed BAM run, except in the case of LWCF over the southern storm track (40°–60°S).

Outside of the tropics CAM5 exhibits smaller resolution sensitivity than the default CAM4. In particular, SWCF shows little resolution sensitivity and is in good agreement with CERES-EBAF. Global mean SWCF in CAM5 0.23 × 0.31 is −46.8 $W m^{-2}$ compared with −47.1 $W m^{-2}$ in CERES-EBAF (Table 1). LWCF biases with respect to CERES-EBAF are somewhat larger than in CAM4 0.9 × 1.25. Nevertheless, the resolution sensitivity of CAM5 LWCF at mid and high latitudes is smaller than for the default CAM4. Poleward of 20° LWCF in CAM5 0.23 × 0.031 is only 2–3 $W m^{-2}$ lower than in the CAM5 0.9 × 1.25 run, while CAM4 using default physics showed a 5–10 $W m^{-2}$ resolution-related drop in LWCF.

While CAM5 radiative fluxes appear generally less sensitive to resolution in mid and high latitudes than CAM4, there are still troubling sensitivities in the tropics, where both SWCF and LWCF weaken by 5–10 $W m^{-2}$ or more at 0.23 × 0.31. This reduction is somewhat stronger with the prescribed BAM configuration, especially for LWCF. However, the effect of resolution is dominant. Overall CAM5 global LWCF is not as well tuned as CAM4's (Table 1). The prescribed BAM run at 0.23 × 0.31 yields a significantly biased global LWCF, 17.2 versus 26.5 $W m^{-2}$ in CERES-EBAF. This exacerbates a bias in LWCF that was already present in CAM5 at 0.9 × 1.25. CAM5's LWCF biases are compensated by a significant 5–6 $W m^{-2}$ clear-sky longwave bias present at both resolutions.

For the rest of the paper we will focus on results from the 25-yr simulations. Unless otherwise specified, whenever "CAM4 0.23 × 0.31" is used it will refer to the high-resolution CAM4 run with modified ice particle sizes, and "CAM5 0.23 × 0.31" will refer to the high-resolution CAM5 run using prescribed BAM aerosols.

4. Model climatology

a. Taylor diagrams

Taylor diagrams (Taylor 2001) provide a concise summary of model performance. Figures 2 and 3 show a selection of Taylor diagrams for important simulation parameters. Each panel shows four symbols. Blue symbols indicate CAM5 results and red symbols indicate CAM4. Filled circles show results from 0.9 × 1.25 simulations and crosses show results from 0.23 × 0.31 simulations. The angle between the x axis and the vector connecting the symbol and the origin indicates the spatial correlation between the simulated and observed fields. The distance from the origin indicates the RMS variability in the simulations normalized by that in the observations. Perfect agreement with verification data, with mean biases removed, would appear as a symbol plotted at (1, 0). Movement closer to (1, 0) between two simulations indicates improvement. Diagrams for December–February (DJF) are shown in Fig. 2 and for June–August (JJA) in Fig. 3.

Quantities associated with the model's global-scale momentum field, such as global sea level pressure over ocean (PSL Ocean), and zonal wind at 200 and 850 hPa

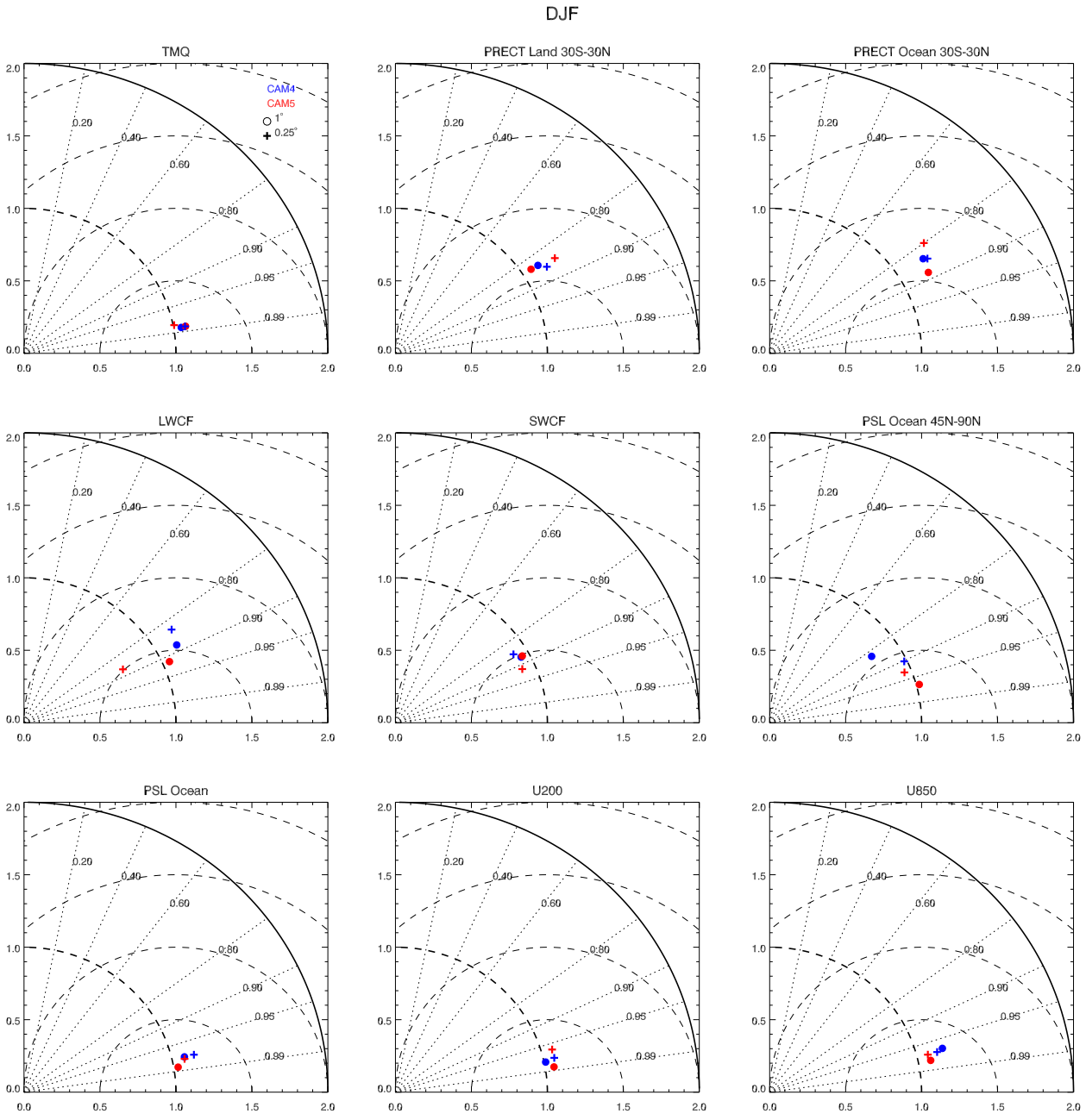

FIG. 2. Taylor diagrams (see text) for several key simulation parameters. Correlations and normalized RMS are calculated using simulated seasonal means for DJF. Blue symbols indicate CAM4 results and red symbols indicate CAM5 results. Filled circles show results for 0.9×1.25 resolution and crosses indicate 0.23×0.31 resolution. Each panel shows a Taylor diagram for a single quantity. Beginning at top left: total precipitable water ; precipitation over land, 30°S–30°N; precipitation over ocean, 30°S–30°N; global longwave cloud forcing; global shortwave cloud forcing; sea level pressure over ocean between 45° and 90°N; global sea level pressure; global zonal wind at 200 hPa; and global zonal wind at 850 hPa.

(U200 and U850) are well simulated in all four model configurations, with correlations above 0.95 and normalized RMS deviations close to 1.0. Total precipitable water (TMQ) follows this pattern as well. For the 0.9×1.25 simulations, most of these fields exhibit noticeable improvements going from CAM4 to CAM5, especially U850 and PSL Ocean. However, systematic improvements from increased resolution are not present.

Regional effects from changes in model physics and model resolution may be more pronounced. Sea level pressure over ocean in northern high latitudes (PSL Ocean 45°–90°N) during DJF exhibits interesting responses to

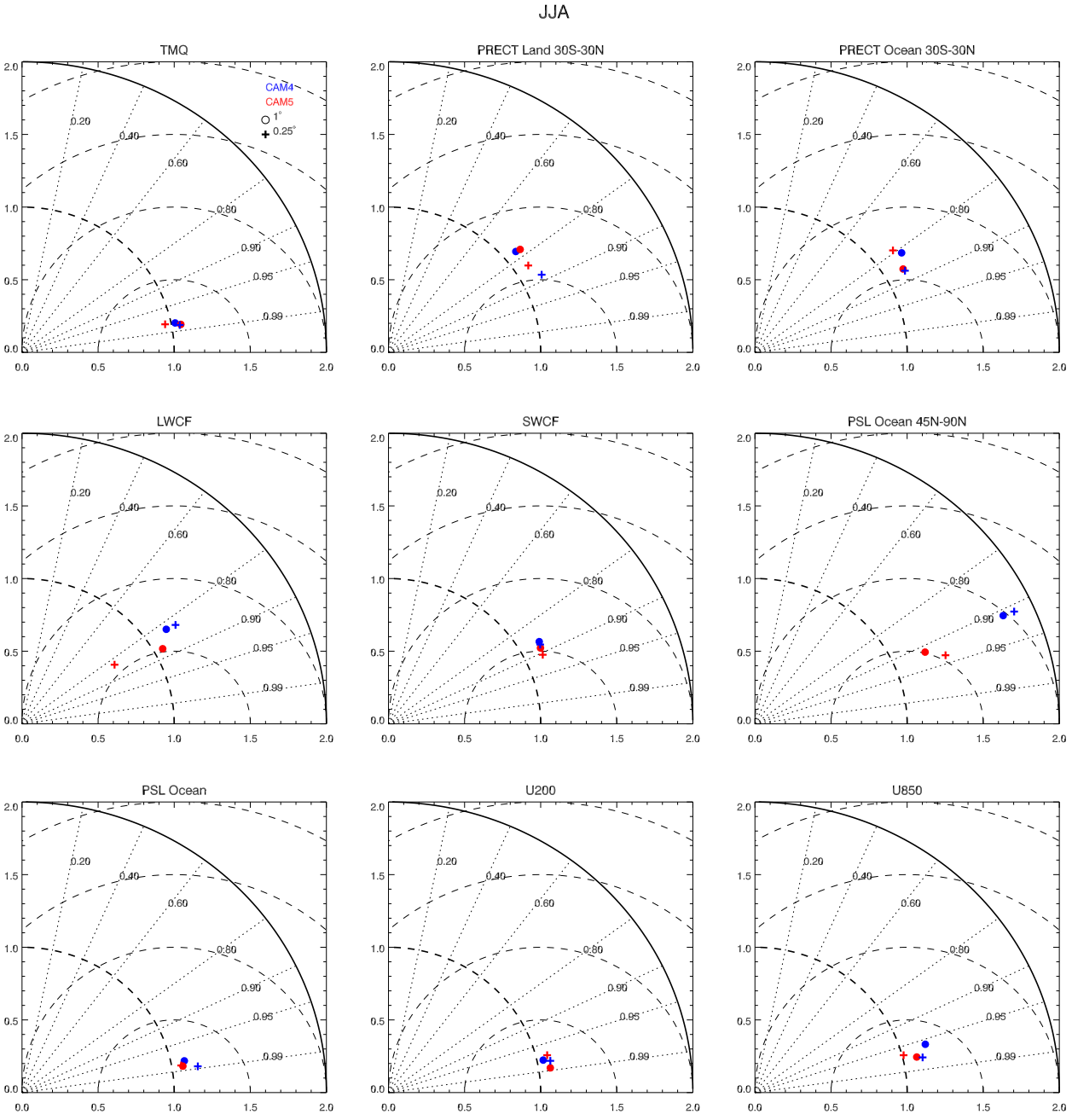

FIG. 3. As in Fig. 2, but for JJA.

both resolution and model physics. In DJF this quantity is best simulated in CAM5 0.9 × 1.25 and most poorly simulated in CAM4 0.9 × 1.25. The improved simulation in CAM5 may be related to the introduction of an orographic enhancement to the surface drag parameterization—"turbulent mountain stress" (TMS; Richter et al. 2010) in CAM5. This drag functions in addition to parameterized drag from unresolved vertically propagating gravity waves and is intended to capture low-level drag from subgrid orography. Interestingly, the simulations of northern winter polar PSL Ocean in CAM4 and CAM5 converge as resolution is increased to 0.23 × 0.31, with CAM5 degrading noticeably while CAM4 improves. This suggests that TMS tuned at 0.9 × 01.25 in CAM5 may hurt simulations at higher resolution, while higher resolution helps CAM4 to better resolve the topographic effects meant to be parameterized by TMS. The role of resolved orographic drag,

parameterized gravity wave drag, and TMS is examined in more detail by Richter et al. (2010) and Lauritzen et al. (2012a), Lauritzen et al. also introduce consistent methods for specifying mean surface topography and subgrid-scale topographic variance in CAM on arbitrary grids.

Quantities associated with cloud physics or moist physics are less well simulated in all configurations, and their Taylor diagrams exhibit more spread, as well as more variability from DJF to JJA. As might be expected, the Taylor plot for LWCF in CAM5 shows large changes in as resolution increases. The major difference is in the normalized RMS deviation rather than correlation, which remains high, 0.8–0.9. Note that although CAM5 0.9 × 1.25 LWCF possesses larger mean biases with respect to CERES-EBAF than CAM4 0.9 × 1.25, it is closer to (1, 0) in the corresponding Taylor diagram, suggesting an improved spatial pattern in simulation of LWCF.

Taylor diagrams for precipitation (PRECT) are shown for 30°S–30°N and separated into land and ocean components. Over ocean, the 0.9 × 1.25 simulations improve with the transition from CAM4 to CAM5 physics. In JJA, ocean precipitation in CAM4 also exhibits a large improvement related to increased resolution, while CAM5 exhibits a nearly opposite deterioration related to increased resolution. In DJF, resolution appears to have little impact on CAM4 ocean precipitation, while in CAM5, again, higher resolution is seen to lead to a substantial deterioration in simulated ocean precipitation. Land precipitation is a field in which substantial improvement with resolution might have been expected, because of better representation of topography. In JJA this is in fact the case, particularly for CAM4, for which pattern correlations with GPCP approach 0.9. For DJF the impact of resolution on land precipitation is less clear. Pattern correlations change little, but normalized RMS becomes larger, particularly in CAM5.

b. *Zonal wind fields*

Seasonal-mean zonal winds at 200 hPa for DJF averaged from December 1980 through February 2005 are shown in Fig. 4 for all four Atmospheric Model Intercomparison Project (AMIP)-style simulations as well from the European Centre for Medium-Range Weather Forecasts (ECMWF) Interim Re-Analysis (ERA-Interim). From the Taylor diagrams in Fig. 2 we expect minor overall differences among the model configurations. This is the case in the extratropics. CAM5 0.9 × 1.25 appears slightly closer to reanalysis than the other three configurations in northern high latitudes, especially over the North Pacific, which is likely reflected as a modest shift toward (1, 0) in the Taylor diagram for U200 in Fig. 2. Both CAM4 and CAM5 exhibit increased easterly bias in the tropics at 0.23 × 0.31, with the most pronounced bias in CAM5 where the equatorial "westerly saddle" (180°–90°W) has nearly disappeared, and equatorial easterlies over South America are 5–10 m s^{-1} stronger than in the other three configurations.

Figure 5 shows seasonal-mean, areally averaged, equatorial zonal wind profiles for DJF from the four AMIP runs. Figure 5a shows corresponding zonally averaged profiles between 10°S and 10°N. The profile for CAM5 0.23 × 0.31 in Fig. 5a is a distinct outlier. Between 400 and 200 hPa the other three configurations as well as ERA-Interim exhibit a layer of westerly shear that begins with winds near −5 m s^{-1} at 400 hPa and ends with winds near 5 m s^{-1} at 200 hPa. This shear layer is almost entirely absent in CAM5 0.23 × 0.31.

Figure 5b shows a regional average over the equatorial Indian Ocean and western Pacific (10°S–10°N, 40°–160°E). Zonal wind profiles in this region have been linked to modifications of equatorial wave dynamics that could influence the dynamics of the Madden–Julian oscillation (MJO) (Roundy 2012). Regionally averaged zonal wind profiles over the equatorial Indian Ocean exhibit the opposite sense of shear to the zonally averaged profiles, with strong (~15 m s^{-1}) easterlies in the upper troposphere and weak easterlies or even westerlies at around 800 hPa. Roundy (2012) suggests that low-level westerlies may connect Kelvin wave dynamics and MJO oscillations. The CAM5 0.23 × 0.31 zonal wind profile in the equatorial Indian Ocean is again the outlier, with 3 m s^{-1} stronger easterlies near 800 hPa than the other three configurations.

c. *Sea level pressure*

The Taylor diagram for wintertime sea level pressure in northern high latitudes (Fig. 2; PSL Ocean 45°–90°N) shows significant differences between configurations, with CAM5 0.9 × 1.25 clearly obtaining the best simulation, CAM4 0.9 × 1.25 the worst, and the high-resolution simulations falling in between. Figure 6 shows the mean seasonal sea level pressure in the north polar region for DJF averaged between 1980 and 2005. Compared with that in CAM4 0.9 × 1.25 (Fig. 6a), the sea level pressure in CAM5 0.9 × 1.25 (Fig. 6b) is in remarkably good agreement with the ERA-Interim reanalysis (Fig. 6e). The relative strengths of the Icelandic and Aleutian lows are well reproduced, as is the high pressure ridge extending from the Beaufort Sea to the East Siberian Sea. CAM4 0.23 × 0.31 exhibits some improvement over its low-resolution counterpart, with a stronger Beaufort/East Siberian Sea high pressure ridge and a weaker Icelandic low. However, the Aleutian low

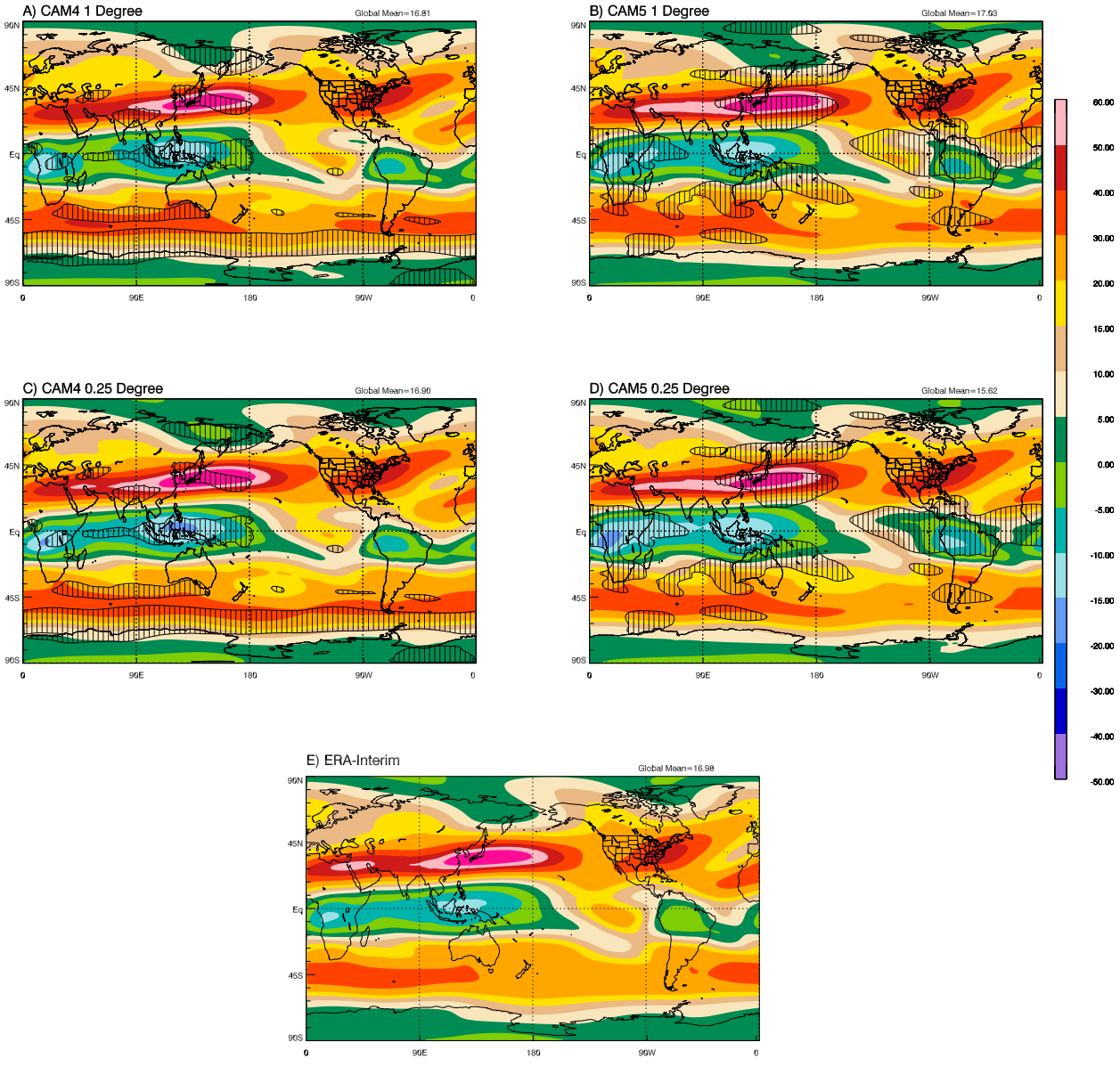

FIG. 4. Seasonal mean zonal wind at 200 hPa as a function of lat and lon for DJF 1980–2005 for (a) CAM4 0.9 × 1.25 resolution, (b) CAM5 0.9 × 1.25 resolution, (c) CAM4 0.23 × 0.31 resolution, (d) CAM5 0.23 × 0.31 resolution, and (e) ERA-Interim. Hatching indicates where differences between the 0.9 × 1.25 and 0.23 × 0.31 simulations are significant at the 90% confidence level using the one-sided Student's *t* test.

becomes too strong. On the other hand, CAM5 0.23 × 0.31 is clearly inferior to its low-resolution counterpart, with a weaker Beaufort Sea high and an unrealistically strong Icelandic low. As discussed in section 3a, this may reflect the fact that CAM5 employs a parameterization of low-level drag that has been tuned for 0.9 × 1.25.

d. Precipitation patterns

Figures 7 and 8 show simulated seasonal mean precipitation distributions compared with GPCP observational estimates. As suggested by the Taylor diagrams in Figs. 2 and 3 the impact of resolution is mixed. Both models show a somewhat exacerbated "double ITCZ" bias pattern at 0.23 × 0.31 compared with 0.9 × 1.25 resolutions, with diminished equatorial precipitation in the Pacific warm-pool and Maritime Continent, and stronger, more extensive ITCZs in the Southern Hemisphere. This is especially evident in the JJA patterns for CAM5 (Figs. 8b,d). Both models at 0.23 × 0.31 also exhibit more intense precipitation in northern ITCZ across the

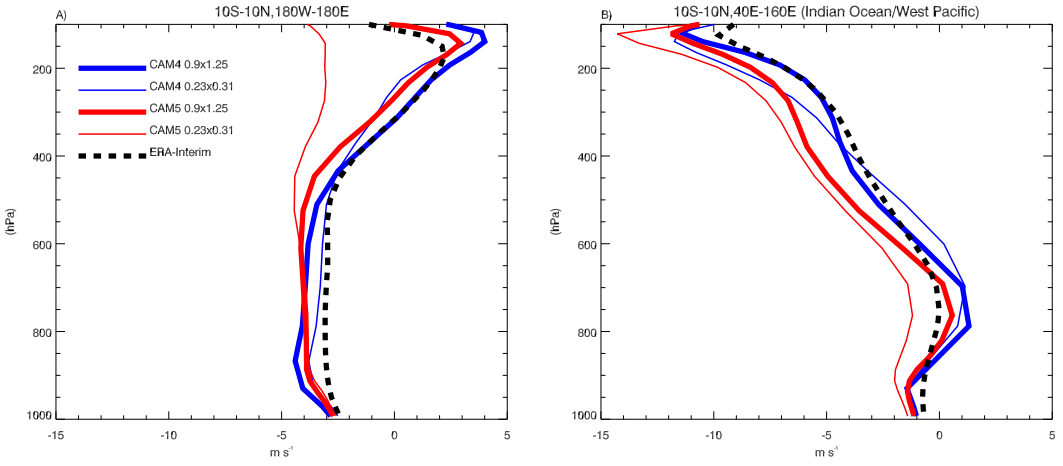

FIG. 5. Seasonal mean, area-averaged zonal wind profiles as a function of pressure for DJF 1980–2005 for (a) a zonal band between 10°N and 10°S and (b) a region including the equatorial Indian Ocean and western Pacific, bounded by 10°N–10°S and 40°–160°E. Blue lines show CAM4 profiles, with thick blue lines showing results for the 0.9 × 1.25 configuration and the thin blue lines for the 0.23 × 0.31 configuration. Red lines show CAM5 profiles; thick red lines the 0.9 × 1.25 configuration, and thin red lines the 0.23 × 0.31 configuration. Dashed black lines show profiles derived from ERA-Interim.

Pacific, magnifying a tropical wet bias that is already present in the 0.9 × 1.25 simulations. On the other hand, the simulation of precipitation in the Indian Ocean during JJA is notably better in CAM4 0.23 × 0.31 than in CAM4 0.9 × 1.25 (Figs. 7b,d). At low resolution, large wet biases are present off the western coast of India, and in the Bay of Bengal, which are significantly reduced in the high-resolution experiment. This improvement, coupled with only modest exacerbation of the double ITCZ bias, leads to the resolution-related improvement in the Taylor score obtained by CAM4 in JJA (Fig. 3).

Over land, significant changes in precipitation are seen over Africa and South America for both models and for both seasons. Generally, the changes associated with increased resolution appear to be positive in JJA with, for example, increased precipitation in the Sahel and sub-Saharan central Africa, where the 0.9 × 1.25 simulations in both models show a dry bias. During DJF the changes associated with increased resolution are mixed. In CAM4 0.23 × 0.31, precipitation rates over southern Africa are weaker and in somewhat better agreement with GPCP than in CAM4 0.9 × 0.125. On the other hand, CAM5 0.23 × 0.31 has stronger precipitation over southern Africa in DJF, and thus an increased bias with respect to GPCP, compared to CAM5 0.9 × 1.25.

Overall, precipitation patterns do not exhibit substantial improvement in either model as resolution is increased. Both models show increased double-ITCZ bias as well as an exacerbated wet bias in the northern ITCZ at 0.23 × 0.31. The most pronounced resolution-related improvement appears to be in precipitation associated with the summer Indian monsoon in CAM4. In CAM5 this feature does not improve dramatically with resolution, in part because it is already better simulated at 0.9 × 1.25 than it is in CAM4. In some respects our results are similar to those of Jung et al. (2012). While they note some improvements in tropical precipitation, their Fig. 5 also shows a significant worsening of the double-ITCZ bias in their model going from spectral T159 to T511 resolution.

The reasons for the strengthening ITCZ biases at 0.23 × 0.31 are not yet well understood. Studies using other AGCMs (e.g., Bacmeister et al. 2006), as well as recent unpublished simulations using CAM5 (D. Williamson 2013, personal communication), suggest that excessive low-level moist heating associated with precipitation leads to excessive coupling between precipitation and low-level convergence. This coupling then leads to enhanced mean moisture convergence and precipitation in simulated ITCZs. Mean moist heating profiles over the North Pacific ITCZ (not shown) from both CAM4 and CAM5 do in fact show increased heating between 900 and 600 hPa in the 0.23 × 0.31 runs.

Establishing a clear connection between the heating profiles and precipitation biases, as well as explaining why heating profiles change with resolution in the first place, will require detailed analysis beyond the scope of this paper. As we will show below, the fraction of large-scale precipitation becomes larger at high resolution, especially for intense rain rates. We speculate that intense large-scale rain is associated with strong condensational heating and weak evaporative cooling at low levels resulting from high low-level humidity.

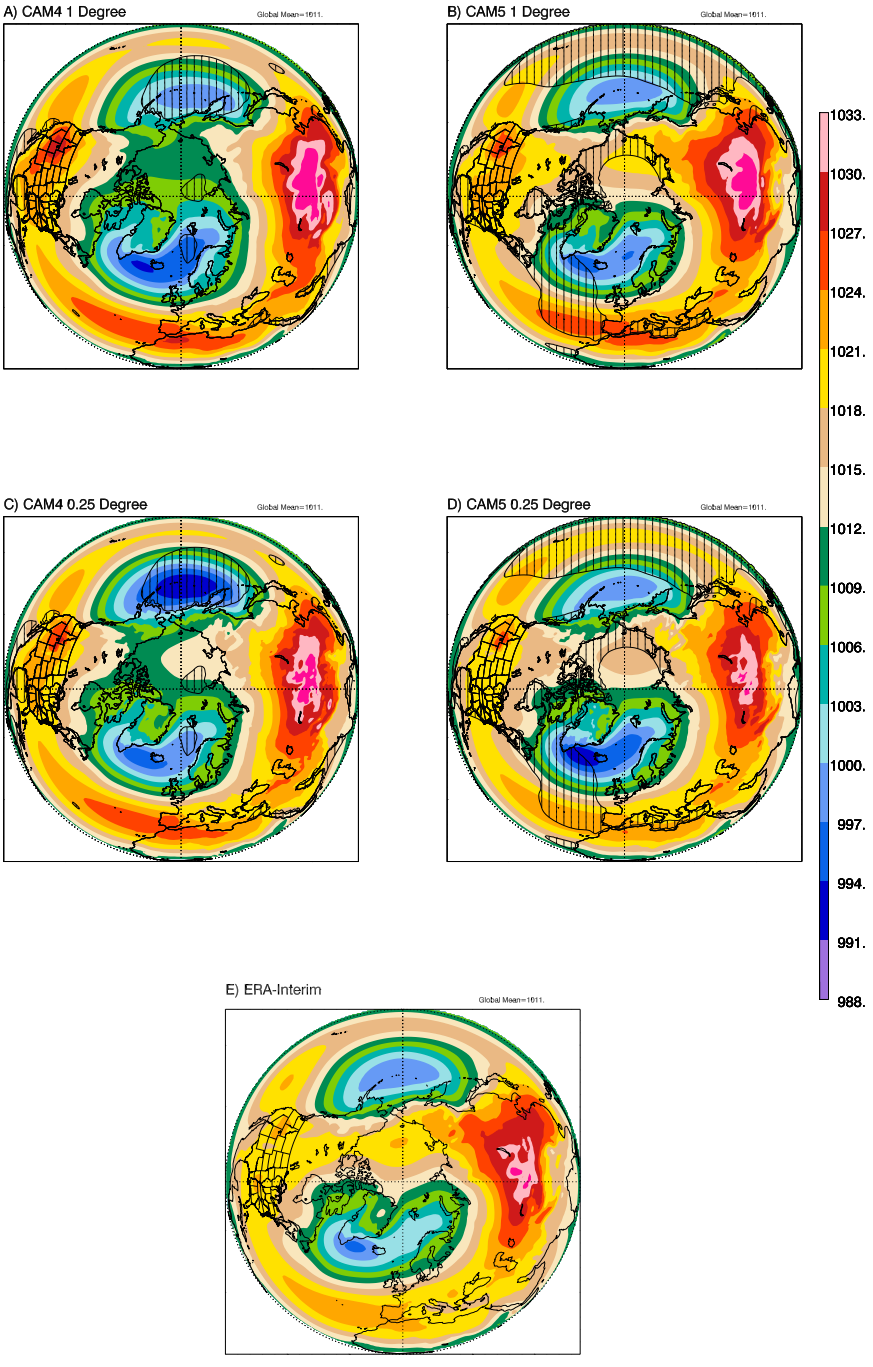

FIG. 6. Seasonal mean sea level pressure as a function of lat and lon for DJF 1980–2005 for CAM4 and CAM5 at (a),(b) 0.9 × 1.25 resolution and (c),(d) 0.23 × 0.31, and (e) ERA-Interim. Hatching indicates where differences between the 0.9 × 1.25 and 0.23 × 0.31 simulations are significant at the 80% confidence level using the one-sided Student's *t* test. Significance is only shown over ocean.

e. Large-scale versus convective precipitation

The fraction of large-scale versus convective precipitation is straightforward to define in models, but is difficult to define observationally. Comparisons of Intergovernmental Panel on Climate Change (IPCC) Fourth Assessment Report (AR4) climate model simulations and TRMM estimates of this ratio have been made (e.g., Dai 2006) and suggest that models produce excessive fractions of convective precipitation. While not easily observed, this ratio is a potentially useful diagnostic of model behavior.

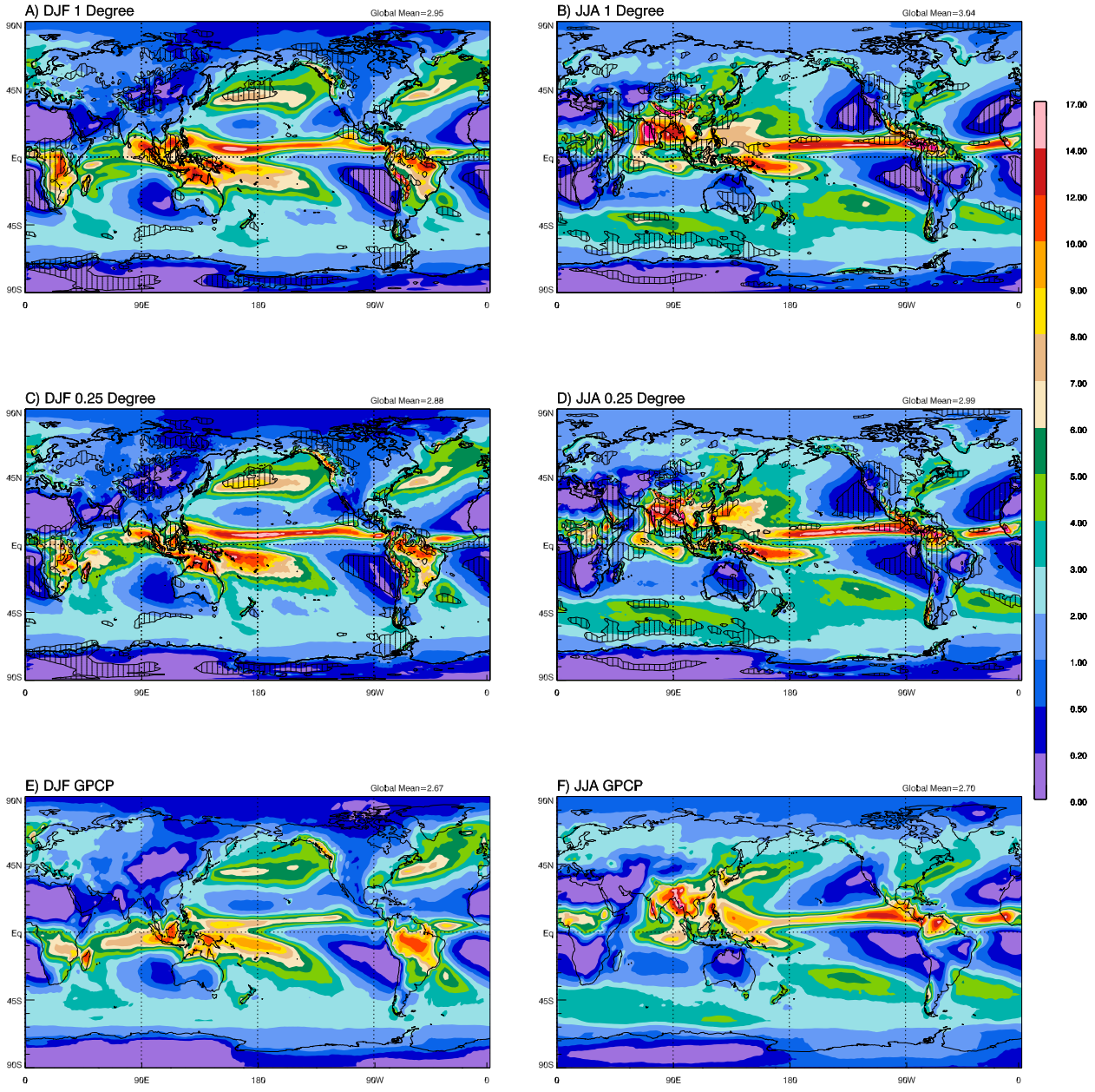

FIG. 7. Seasonal mean precipitation climatology averaged from 1980 to 2005 in CAM4 at 0.9 × 1.25 resolution for (a) DJF and (b) JJA; CAM4 at 0.23 × 0.31 resolution for (c) DJF and (d) JJA; and GPCP estimate for (e) DJF and (f) JJA. Hatching indicates where differences between the 0.9 × 1.25 and 0.23 × 0.31 simulations are significant at the 90% confidence level using the one-sided Student's *t* test.

Figure 9 shows zonal means of annually averaged total precipitation in all four AMIP simulations along with zonal means of the large-scale component of the precipitation. Table 2 summarizes results from the figure. Note the excessive tropical precipitation in both versions of CAM at both high and low resolution. In both CAM4 and CAM5 the ratio of large-scale precipitation increases as resolution increases. The ratio of large-scale to total precipitation is lower in CAM5 than in CAM4 at comparable resolution, with the tropical ratio over 50% in CAM4 0.23 × 0.31 and close to 30% in CAM5 0.23 × 0.31. In this respect, CAM4 is clearly closer than CAM5 to TRMM observational estimates (e.g., Dai 2006), which characterize less than half of tropical precipitation as convective.

f. Precipitation intensity statistics

Intensity statistics for precipitation in global models are well known to suffer from serious deficiencies (Dai 2006; Stephens et al. 2010). The frequency of weak to

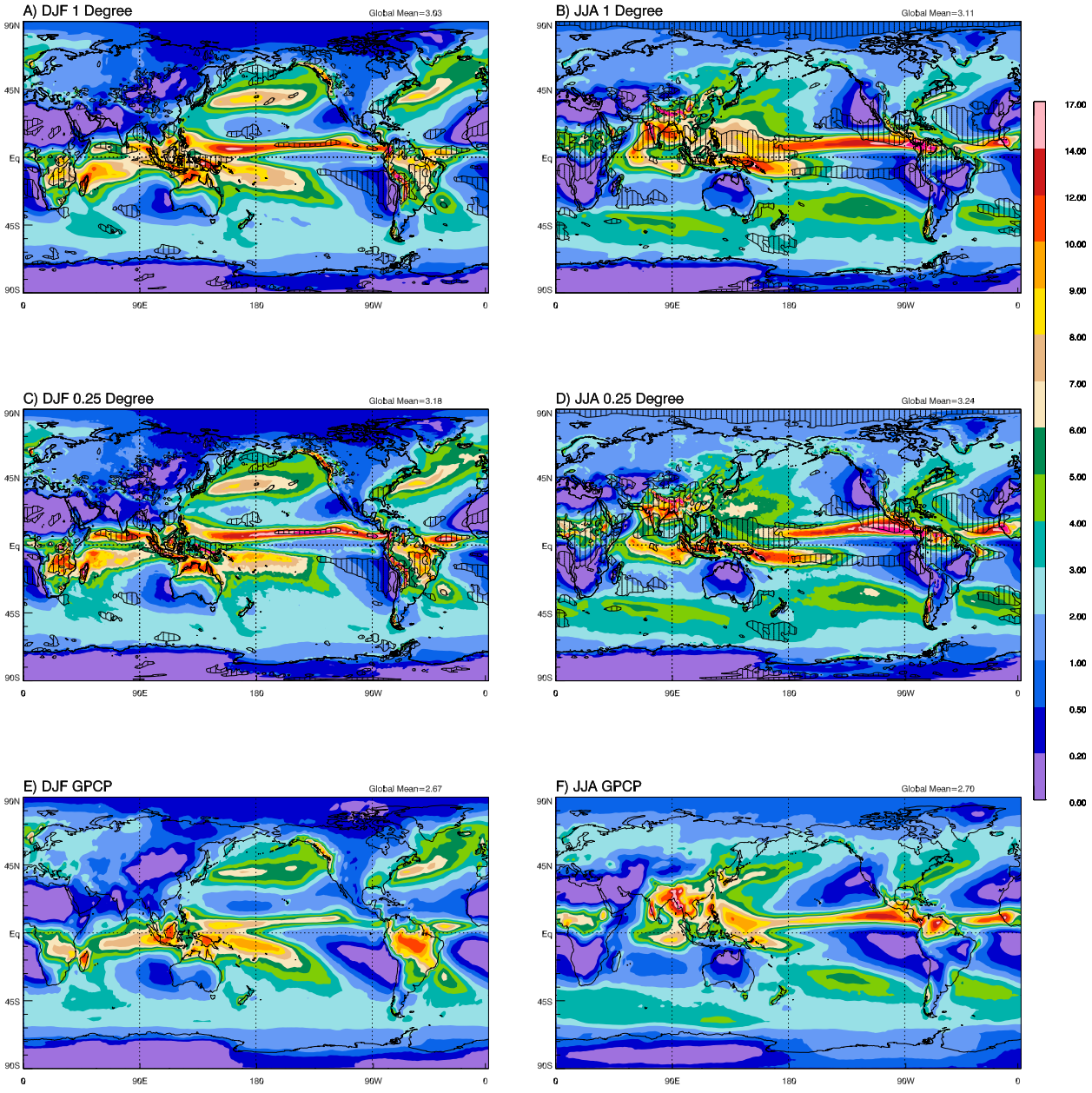

FIG. 8. As in Fig. 7, but for CAM5.

moderate precipitation is overestimated in models, while intense events may be underrepresented, although there are suggestions that CAM at 0.23 × 0.31 may also overestimate the frequency of extreme precipitation rates (Boyle and Klein 2010; Bacmeister et al. 2012). Figure 10 shows probability density functions (PDFs) of 3-hourly averaged precipitation intensity between 30°S and 30°N accumulated over 3 months (June–August 2005) from CAM4 and CAM5 and from TRMM 3B42 observational estimates. Note that TRMM 3B42 and results from the 0.23 × 0.31 simulations are comparable because of their similar horizontal and temporal resolution.

The major differences between the simulated PDFs and the observational estimate from TRMM 3B42 are excessive probability of precipitation rates $<30\,\mathrm{mm\,day^{-1}}$ and deficient probability of rates between 30 and $500\,\mathrm{mm\,day^{-1}}$. As has been noted elsewhere (Bacmeister et al. 2012), CAM5 0.23 × 0.31 overestimates the frequency of intense precipitation ($>500\,\mathrm{mm\,day^{-}}1$) relative to TRMM. By contrast, our CAM4 0.23 × 0.31 experiment does not appear to overestimate the frequency of

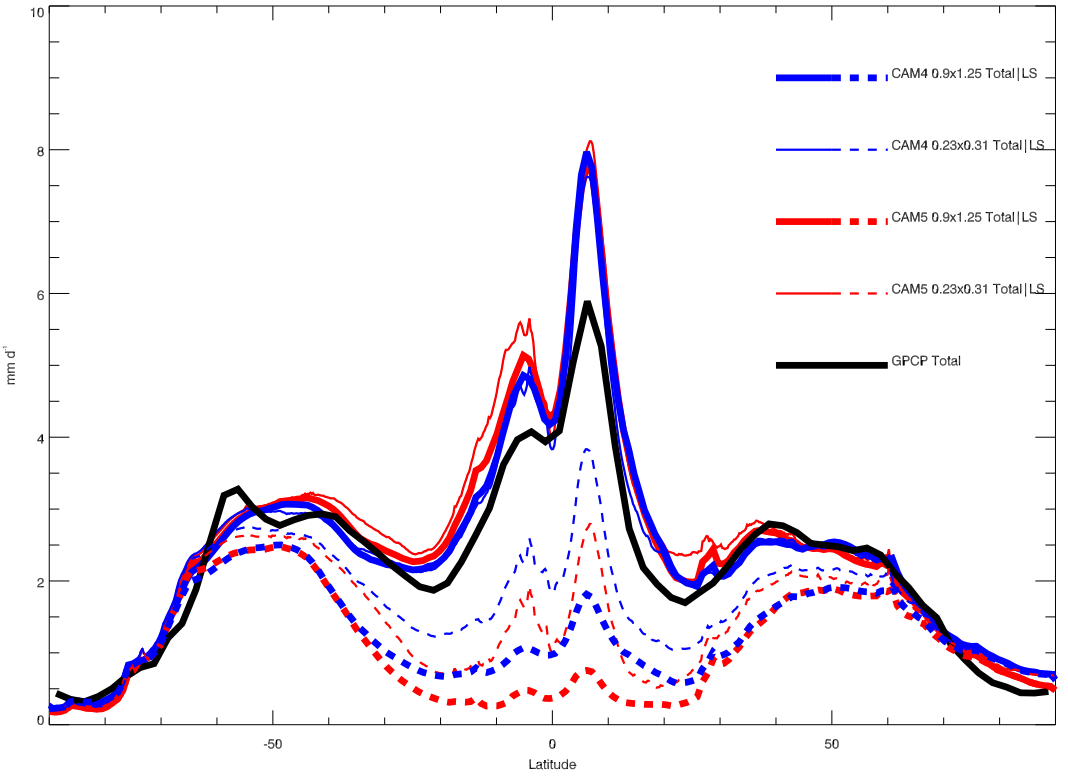

FIG. 9. Zonal mean, annually averaged precipitation for 1980–2004 as a function of lat. Solid lines show total precipitation with red indicating CAM5 results, blue indicating CAM4, and black showing GPCP observational estimates. Thin lines show results for 0.23 × 0.31 resolution and thick lines show results for 0.9 × 1.25. Dashed lines show large-scale component of precipitation.

intense events compared to TRMM, although Boyle and Klein (2010) report that short-term forecast runs using CAM4 at 0.23 × 0.31 do overestimate the occurrence of rain rates >100 mm day^{-1} compared with local ground-based radar observations.

Precipitation in higher-resolution models could exhibit higher frequency of intense rates simply because individual rain events become more concentrated, while mean rain rates at larger spatial scales remain unchanged. To examine this possibility, we coarse grained the 3-hourly precipitation from CAM5 0.23 × 0.31 to a 0.9 × 1.25 grid before calculating the PDF. This PDF of coarse-grained precipitation (Fig. 10, dashed red line) continues to show much more frequent precipitation at rates >40 mm day^{-1} than the native CAM5 0.9 × 1.25 result (Fig. 10, thick red line).

All of the configurations examined here exhibit excessive probabilities for weak-to-moderate precipitation rates (<30 mm day^{-1}) compared to TRMM 3B42. Probabilities of these rates are up to an order of magnitude greater than in the observational estimate. Little variation exists among the models in this intensity regime. Figure 11 shows the contribution of convective precipitation (including both shallow and deep contributions) to the intensity PDFs. It is evident that almost all tropical precipitation with rates below 30 mm day^{-1} originates in the models' shallow and deep convective parameterizations, while almost all of the precipitation with rates >100 mm day^{-1} is produced by the models' large-scale condensation routines. This pattern holds at both low (Fig. 11c) and high resolution (Figs. 11a,b), and suggests that convective precipitation intensity is independent of model resolution. While TRMM 3B42 may underestimate the occurrence of precipitation

TABLE 2. Annually averaged precipitation (mm day^{-1}), total and large-scale for 1980–2004 from CAM4 and CAM5.

	CAM4		CAM5	
	0.9 × 1.25	0.23 × 0.31	0.9 × 1.25	0.23 × 0.31
		30°S–30°N		
Total	3.63	3.47	3.74	3.94
Large scale	0.94	1.75	0.43	1.15
		Global		
Total	2.96	2.88	3.04	3.18
Large scale	1.30	1.88	1.03	1.53

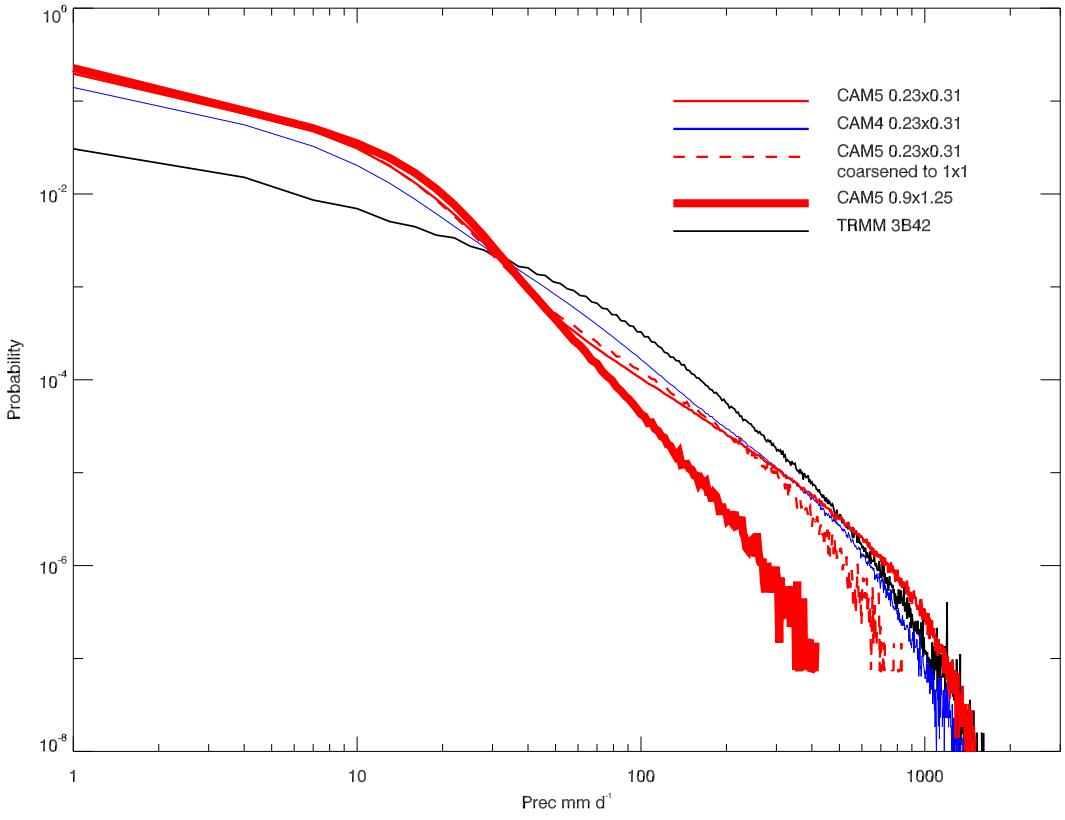

FIG. 10. PDFs of tropical precipitation (30°S–30°N) for JJA 2005. Probabilities are with respect to bins of 3 mm day^{-1}. Red lines show results for CAM5: thick solid line for 0.9 × 1.25; thin solid line for 0.23 × 0.31; and thin dashed line for 0.9 × 0.31 after coarse graining to a 0.9 × 1.25 grid. Thin blue line shows results for CAM4 0.23 × 0.31. Black line shows result from TRMM 3B42 observational estimate.

rates <30 mm day^{-1}, an order-of-magnitude underestimate is unlikely (Stephens et al. 2010). So, the apparent overactivity of CAM's convective parameterizations in producing weak-to-moderate precipitation represents a possibly serious error that does not diminish with resolution. A comprehensive look at the behavior of precipitation extremes in CAM5 can be found in Wehner et al. (2013, manuscript submitted to *J. Adv. Model. Earth Syst.*).

5. Intraseasonal variability

Reasonable simulation of intraseasonal variability (ISV) associated with the MJO has been an elusive target for climate models (Lin et al. 2006) despite the large spatial and long temporal scales involved. Modifications to the deep convection scheme in CAM introduced between versions 3 and 4 (Neale et al. 2008) resulted in a significant improvement in the model's MJO simulation. Figure 12 shows space–time spectra of tropical precipitation emphasizing space–time scales associated with the MJO. Figures 12a and 12b show results for CAM4 and CAM5 at 0.9 × 1.25 resolution. Variability is weak overall compared with TRMM observations (Fig. 12e) and is especially weak at the longer time scales (>20 days) associated with the MJO. CAM4 0.9 × 1.25 exhibits substantially stronger variability than CAM5 0.9 × 1.25. The 0.23 × 0.31 results (Figs. 12c,d) are disappointing for both CAM4 and CAM5, showing generally weaker variability at long time scales than their 0.9 × 1.25 counterparts.

Band-passed (20–90 day) variance, averaged from 10°S to 10°N, is shown in Fig. 12f. Consistent with the wavenumber–frequency spectra, all four CAM runs are weak compared to TRMM in the region of strong MJO activity (40°E–160°W). The models have particular difficulty capturing the Indian Ocean variance peak located near 90°E.

6. Regional precipitation over the United States

An important motivation for conducting high-resolution global climate simulations is to reproduce regional climate regimes and to capture mesoscale circulations that are

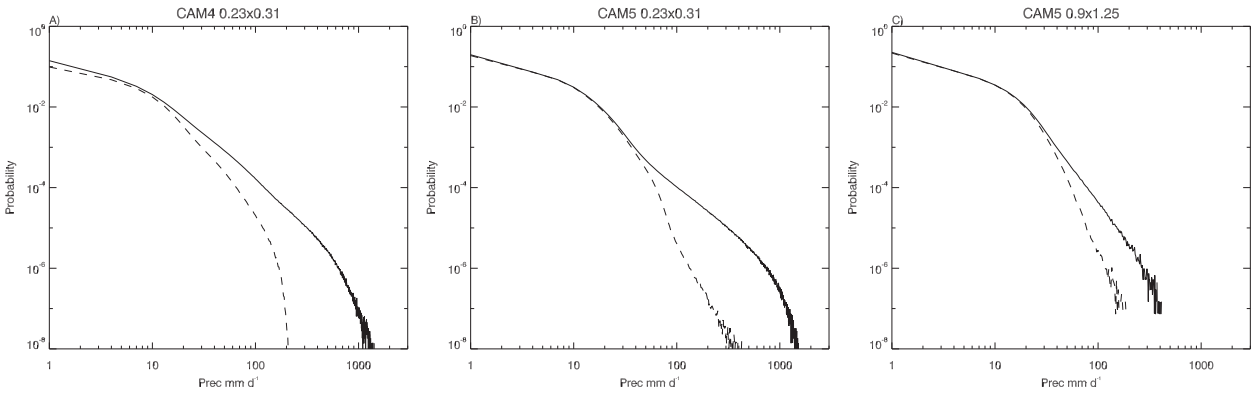

FIG. 11. PDFs of tropical precipitation for (a) CAM4 0.23 × 0.31, (b) CAM5 0.23 × 0.31, and (c) CAM5 0.9 × 1.25. Solid lines show PDFs of total precipitation as in Fig. 10. Dashed lines show PDFs of precipitation produced by deep and shallow convection parameterizations.

capable of producing extreme conditions. Correctly simulating climatological precipitation over the United States is challenging because of the complex dynamics of precipitation in this region. Summertime precipitation is dominated by convective precipitation with organized convection playing a key role in part of the region (Maddox 1980). Wintertime precipitation is dominated by midlatitude cyclonic storms that obtain significant moisture from warm water in the Gulf of Mexico. As we will see below, increasing resolution impacts these regimes in different ways.

Figure 13 shows seasonal mean precipitation from CAM5 at 0.9 × 1.25 and 0.23 × 0.31 resolutions for DJF and JJA. In winter a strong response to increased resolution is evident (Figs. 13a,c), with significantly increased precipitation throughout the southeast United States. This increase alleviates a large dry bias present at lower resolution over most of the Gulf and Ohio Valley states. At the same time a smaller area of wet bias is produced along the southeast Atlantic coast. We observe a similar response to increased resolution in CAM4 (not shown). By contrast, in summer (Figs. 13b,d) increased resolution leads to little change in the seasonal mean precipitation pattern. A serious dry bias is present at both 0.9 × 1.25 and 0.23 × 0.31 over the upper Midwest and central Great Plains states, while a strong wet bias persists over the central Rockies and adjacent high plains.

a. *Wintertime water budget over the southeast United States*

To understand the sensitivity of wintertime precipitation in the southeastern United States to resolution we examined the water budget of a domain bounded between 100° and 80°W and 30° and 40°N (Fig. 14, inset). Figure 14 shows integrated monthly mean precipitation over this domain (in $\mathrm{kg\,s^{-1}}$) as a function of the monthly-mean, integrated, horizontal flux of water vapor (also in $\mathrm{kg\,s^{-1}}$) through its southern edge. Each small symbol plotted represents a monthly mean for December, January, or February between 1980 and 2004. Results for all four AMIP configurations are plotted.

The figure shows that moisture flux across the southern edge of the domain and domain precipitation are highly correlated, with $r > 0.7$ for all four configurations. All four configurations also exhibit a similar relationship between the flux and precipitation, with precipitation at about 40% of the flux in each case. While causality cannot be determined from this analysis, it is tempting to conclude that transport of water vapor from the Gulf of Mexico largely determines precipitation amounts in this domain. A large amount of scatter and overlap among experiments is also present. The climatological means (large symbols) for the 0.9 × 1.25 and 0.23 × 0.31 configurations are statistically different according to a *t* test at 90% confidence (CAM4) and 99% confidence (CAM5), but it is clear that individual months or seasons may not give results consistent with the means.

b. *Diurnal cycle of summertime precipitation*

Figures 15a and 15b show mean CAM5 and TRMM 3B42 precipitation as a function of local time for the two domains indicated in Fig. 15c. The results shown are averages over JJA from 1999 through 2005. In addition to the diurnal cycle of total precipitation, the diurnal cycle of large-scale precipitation is also shown. TRMM estimates in the two domains exhibit very different diurnal cycles. In the upper Midwest TRMM (Fig. 15a) shows a broad but distinct nocturnal peak (1100–1400 LT), which is well known and has been attributed to eastward propagating mesoscale convective complexes or systems (MCCs or MCSs; e.g., Maddox 1980; Carbone et al. 2002; Trier et al. 2006; Tuttle and Davis 2006). The

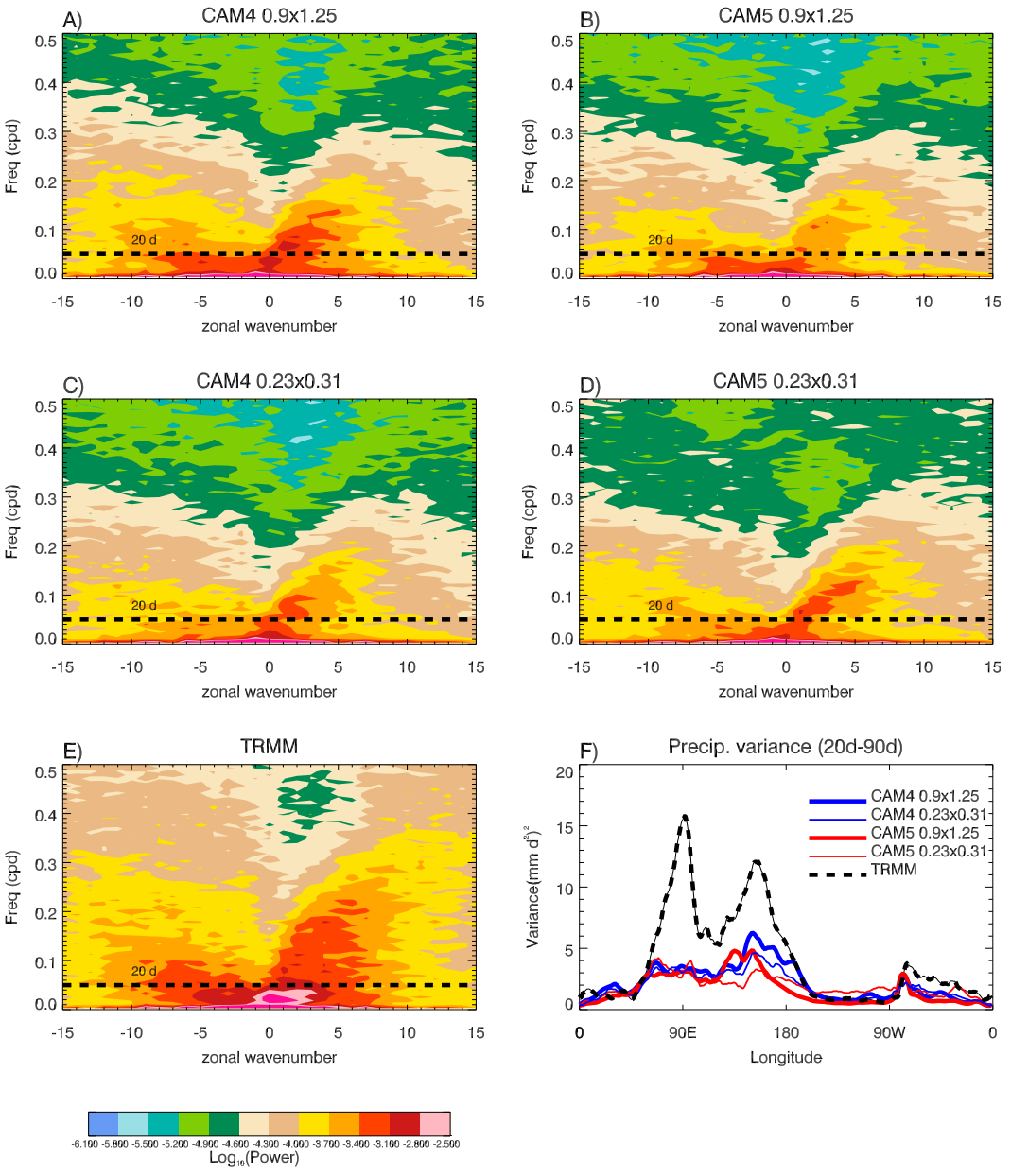

FIG. 12. (a)–(e) Zonal wavenumber–frequency power spectra of daily precipitation averaged from 10°S to 10°N for 1 Jan 1999–31 Dec 2004: (a) CAM4 0.9 × 1.25, (b) CAM5 0.9 × 1.25, (c) CAM4 0.23 × 0.31, (d) CAM5 0.23 × 0.31, and (e) TRMM 3B42 observational estimate. (f) Time mean bandpass-filtered (20–90 day) variance of precipitation for the same period averaged from 10°S to 10°N.

observed diurnal cycle over the southeast United States (Fig. 15b) exhibits the clear late afternoon/early evening peak (1400–1800 LT) that is expected for disorganized ''air mass'' convection.

Unfortunately, the diurnal cycle of CAM5 precipitation does not distinguish between these two domains. In both domains the diurnal cycle peaks in late afternoon as would be expected for disorganized convection. This leads to reasonable agreement between CAM5 and TRMM in the southeastern United States (Fig. 15b). However, over the upper Midwest (Fig. 15a) the simulated diurnal cycle of precipitation is nearly perfectly out of phase with the TRMM observed cycle. Interestingly, the simulated diurnal cycle of large-scale precipitation in the 0.23 × 0.31 runs (thin dashed lines) does show a distinct nocturnal/early morning maximum. At least part of this maximum is contributed by eastward moving features with intense precipitation rates (not shown),

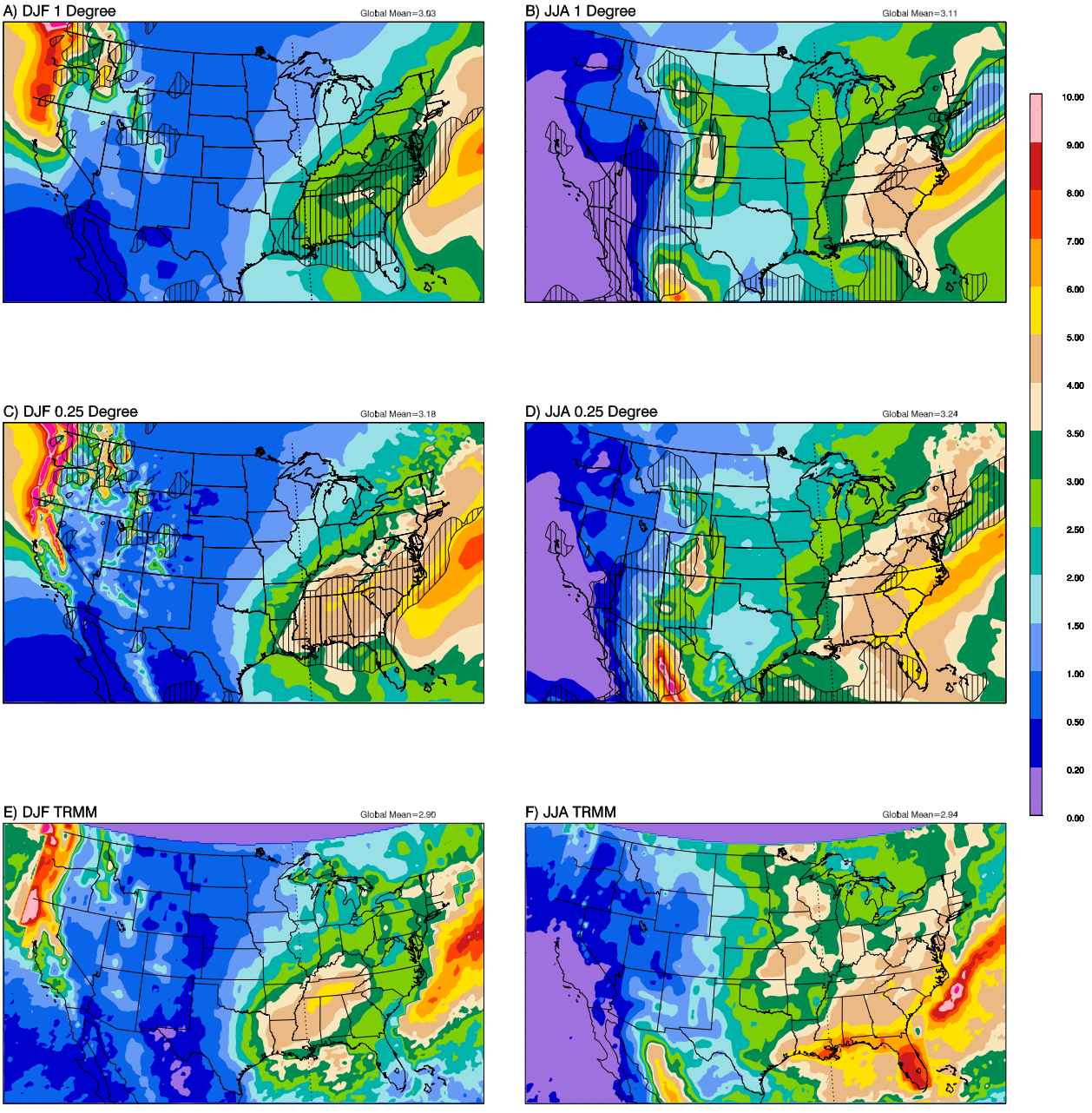

FIG. 13. Seasonal mean precipitation climatology over North America averaged from 1999 to 2005 in CAM5 at 0.9×1.25 resolution for (a) DJF and (b) JJA; CAM5 at 0.23×0.31 resolution for (c) DJF and (d) JJA; and TRMM estimate for (e) DJF and (f) JJA over same period. Hatching indicates where differences between the 0.9×1.25 and 0.23×0.31 simulations are significant at the 90% confidence level using the one-sided Student's *t* test.

with characteristics that superficially resemble those that might be expected of marginally resolved MCCs.

7. Tropical cyclones

a. Numbers and track densities

Climate models running at high resolution are capable of capturing many aspects of the observed tropical cyclone (TC) climatology with reasonable fidelity, including geographical, seasonal, and even interannual variations (e.g., Zhao et al. 2009; Manganello et al. 2012). To identify and track storms, we employ a simple algorithm based on departures from a 14-day mean surface pressure combined with a threshold value of $0.0013\,s^{-1}$ for near-surface vorticity (see the appendix). Results from our algorithm compare well with results

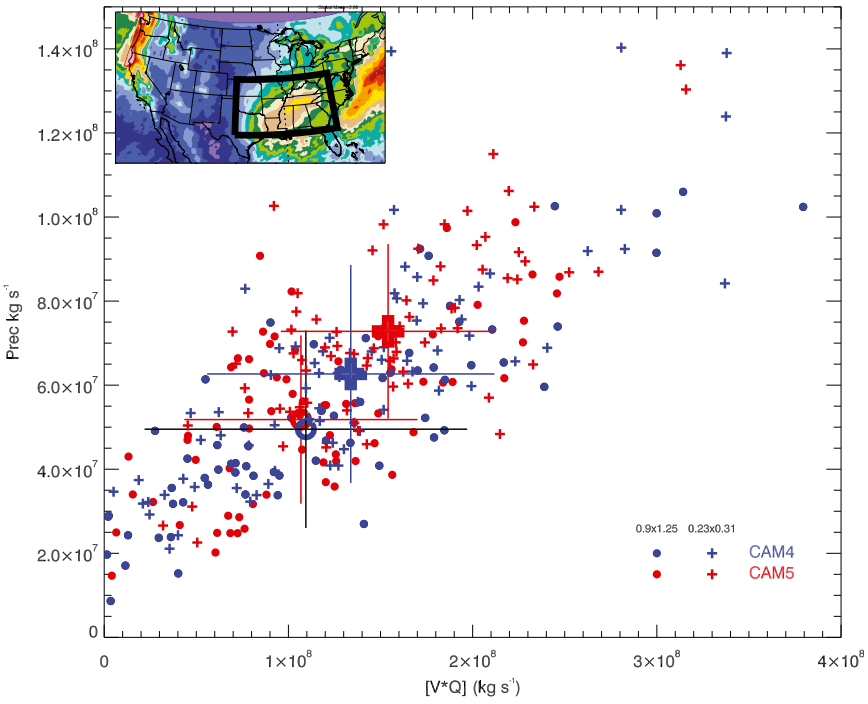

FIG. 14. Total precipitation flux (kg s^{-1}; vertical axis) vs total northward water flux through southern edge (kg s^{-1}; horizontal axis) for southeast United States domain shown in inset map in top left corner. Each small symbol represents a monthly mean for December, January, or February between 1980 and 2005. Blue symbols indicate CAM4 results and red symbols indicate CAM5. Filled circles show results for 0.9 × 1.25 resolution and crosses show results for 0.23 × 0.31. Large symbols show 1980–2005 means with standard deviations shown by horizontal and vertical lines.

from the Geophysical Fluid Dynamics Laboratory (GFDL) tracking algorithm (Vitart et al. 1997; Zhao et al. 2009) in overall storm counts and track densities.

For validation we use data from the International Best Track Archive for Climate Stewardship version 3.4 (IBTrACS v03r04; Knapp et al. 2010). North Atlantic and northeast Pacific track data are taken from the National Hurricane Center hurricane database (HURDAT) and elsewhere Joint Typhoon Warning Center (JTWC) data are used, as in Klotzbach (2006). These data report 1-min wind speeds while model winds represent 15-min averages. A scaling factor of 0.93 is used to convert 1-min observed winds to 10-min values (Harper et al. 2010) for fairer comparison with the simulations. In addition, model winds were saved at the lowest model level, which is situated close to 60 m, while IBTrACS winds represent 10-m values. Accordingly, model winds are scaled using the wind power law (Hsu et al. 1994). Thresholds for storm categories in both the models and observations are reduced to reflect the use of 10–15-min average wind speeds rather than 1-min maximum sustained winds (e.g., Manganello et al. 2012). However, no resolution-based adjustments are used for model storm categories.

Figure 16 shows track densities for various intensity categories in CAM4 and CAM5 compared with densities from IBTrACS. For TCs of any intensity (Fig. 16, left) both models show a generally satisfactory pattern of track densities compared with IBTrACS. Biases include excessive activity in the western North Indian Ocean (including the Persian Gulf) in both CAM4 and CAM5. CAM4 exhibits sharply weaker North Atlantic hurricane activity than CAM5, with CAM5 closer to observed levels. By contrast CAM4 is somewhat more active and closer to observations in northwest Pacific basin. Both models are overactive in the north central Pacific near the date line, possibly related to their ITCZ precipitation biases. CAM5 also exhibits a notable excess of activity in the northeast Pacific. For storms of category 3 and above (Fig. 16, right) both models are underactive in most basins, although CAM5 retains realistic densities in the North Atlantic.

Other models, notably GFDL's high-resolution atmospheric model (HiRAM; Zhao et al. 2009), have shown skill in reproducing observed means and interannual variability in tropical cyclone numbers in the North Atlantic basin. Zhao et al. also show that significant

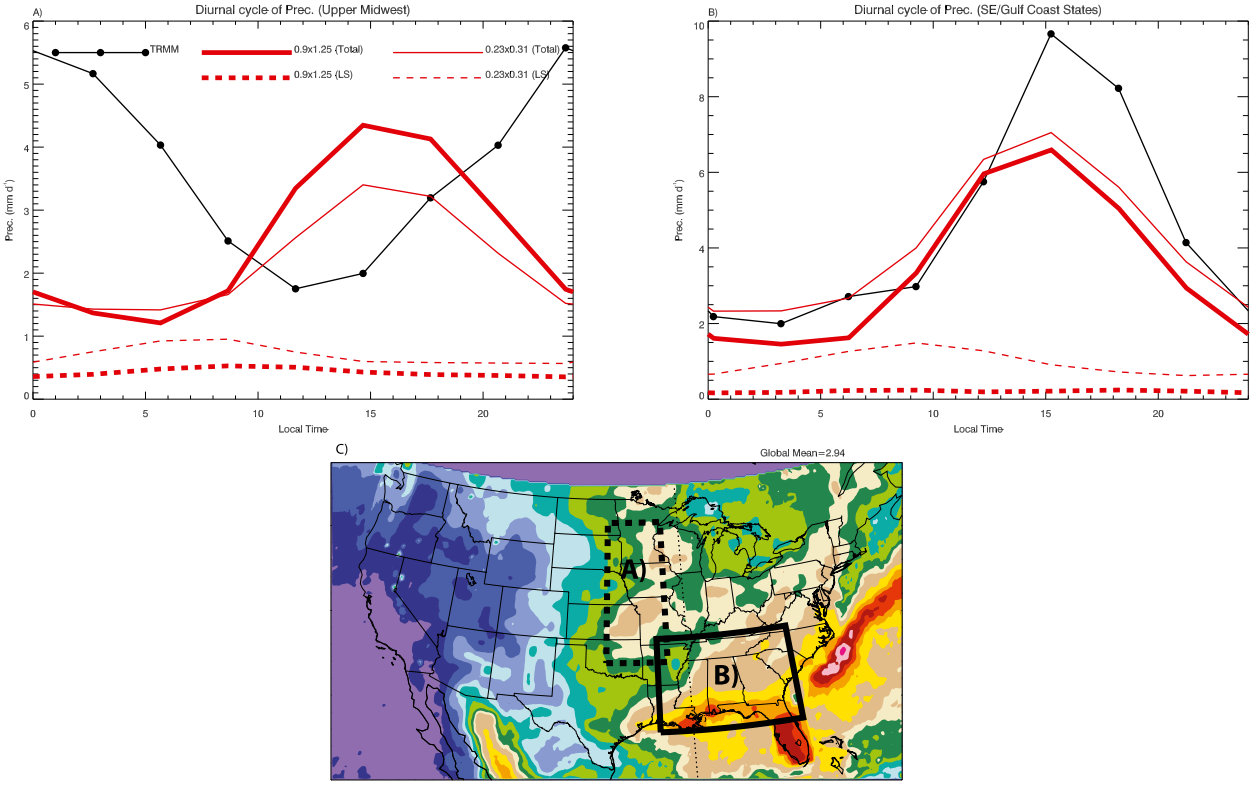

FIG. 15. Mean diurnal cycle of precipitation in CAM5 and TRMM 3B42 for JJA 1999–2005 in the analysis domains of (a) the upper Midwest and (b) the Gulf States/southeast United States. Solid red lines show diurnal cycles for total precipitation CAM5: thick for 0.9 × 1.25 and thin for 0.23 × 0.31. Black lines with filled circles show the cycles of TRMM 3B42 precipitation. The dashed red lines show diurnal cycles of simulated large-scale precipitation in CAM5: thick for 0.9 × 1.25 and thin for 0.23 × 0.31. (c) Map showing the domains for (a) and (b).

ensemble variability TC numbers for individual basins can exist. Nevertheless, our CAM5 1980–2005 integration shows interesting behavior in the North Atlantic basin, so we describe it here. The run exhibits skill in reproducing observed TC numbers over part of the 1980–2005 integration (Fig. 17). Excellent correlation holds for the first 14 yr ($r = 0.73$) but then breaks down over the last 10 yr of the run, yielding an overall correlation $r = 0.16$, well below significance. This result is insensitive to the details of the tracking algorithms used. Observed North Atlantic TC activity in 1995, 1996, and 1998–2005 shows a sustained enhancement that has been attributed to a shift in the Atlantic multidecadal mode (AMM; Goldenberg et al. 2001; Bell and Chelliah 2006; Klotzbach and Gray 2008). TC activity in the North Atlantic during 1997 was likely suppressed by a strong El Niño (e.g., Camargo and Sobel 2005; Camargo et al. 2007). Our CAM5 run does not reproduce this pattern of activity. Instead below average TC counts are simulated from 2000 to 2004, and even more disappointingly North Atlantic activity during the 1997 El Niño is anomalously high.

Some indication of why CAM5 does a poor job of simulating North Atlantic TC numbers after 1995 may come from examining large-scale variables associated with tropical cyclogenesis. We use the genesis potential index (GPI) proposed by Emanuel and Nolan (2004). This index has been shown to have some skill in capturing interannual variability in the North Atlantic (Camargo et al. 2007; Menkes et al. 2012). GPI consists of four factors, two that depend directly on winds, one that depends on relative humidity at 600 hPa, and one that depends on potential intensity (Bister and Emanuel 2002). Our calculation of GPI follows that of Camargo et al. (2007) using monthly mean model winds, temperature, and humidity and an iterative scheme to compute potential intensity. Figure 18 (top) shows time series of GPI averaged over a region bounded by 10°–25°N and 70°–10°W compared with simulated TC numbers in the North Atlantic. Correlations are not high ($r = 0.45$) but are significant. Of particular interest is the fact that the North Atlantic averaged GPI for CAM5 (red dashed line) shows a decreasing trend between 1995 and 2003, generally consistent with the trend in simulated TC

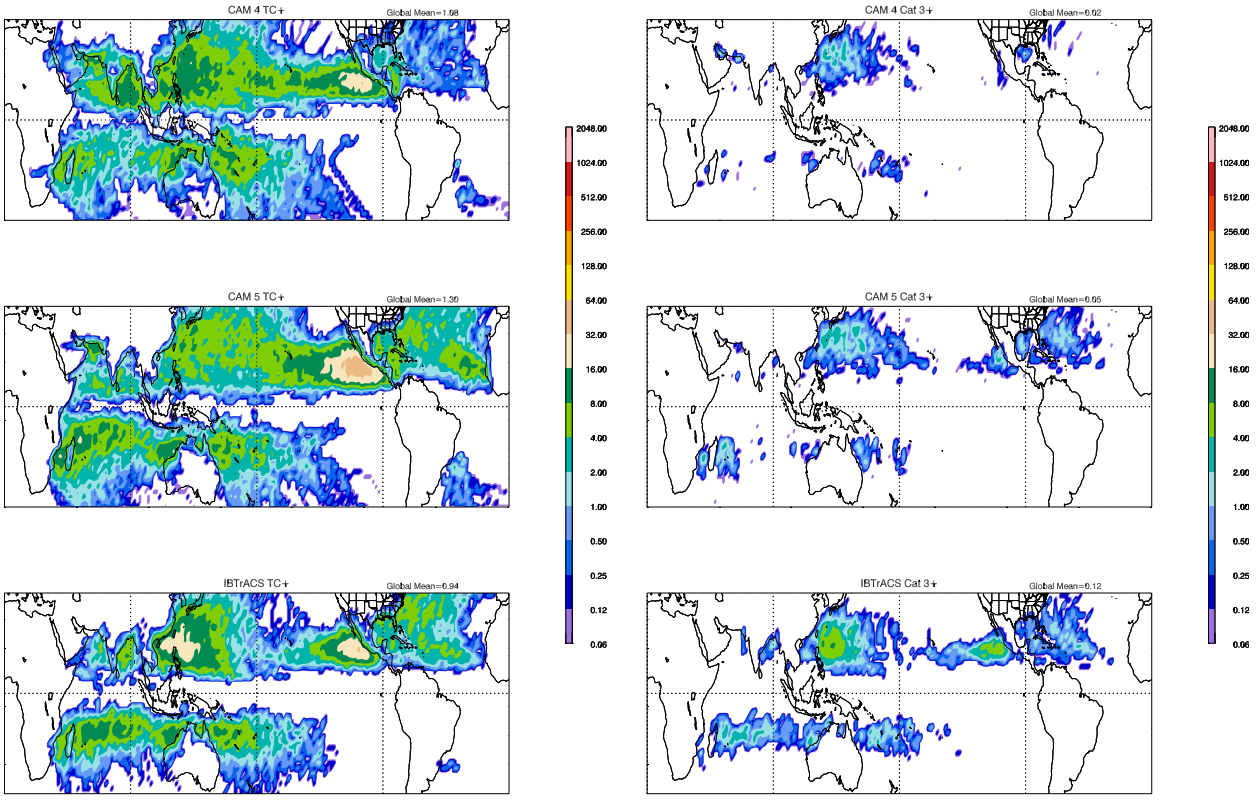

FIG. 16. Mean track densities for 1980–2004 for (left) all tropical cyclones and (right) major storms (category 3 and stronger), in (top) CAM4 0.23 × 0.31, (middle) CAM5 0.23 × 0.31, and (bottom) IBTrACS. Units are mean hours per year when a TC or major storm is found within a 1° × 1° box.

number. This then suggests that the model is generating storm numbers consistent with its mean climate throughout the run. We should point out that the aerosol climatology used to force our CAM5 simulation does not include interannual variations. So, this possible contributor to North Atlantic TC variability (e.g., Dunion and Velden 2004) is missing.

We also examined the time series of the four factors comprising GPI in the CAM5 simulation (Fig. 18, bottom). This analysis suggests that the decline in simulated GPI between 1995 and 2003 is brought about by a decline midtropospheric relative humidity in CAM5. This factor has the highest correlation ($r = 0.43$) with the simulated North Atlantic storm count, and also exhibits a drop between 1995 and 2004.

b. *Accumulated cyclone energy*

Accumulated cyclone energy (ACE; Bell et al. 2000) is another measure of tropical cyclone activity. ACE for a subset B of storms is defined as

$$\mathrm{ACE}_B = 10^{-4} \times \sum_{t \in B} V_{\max}(t), \qquad (2)$$

where $V_{\max}(t)$ is the maximum 6-hourly surface wind in knots ($1\,\mathrm{kt} \approx 0.51\,\mathrm{m\,s^{-1}}$) and the sum is over all 6-h samples for all storms in B. An advantage of ACE is that, given comparable surface wind estimates, it is less sensitive to the details of tracking algorithms than TC number. Figure 19 shows time series of yearly global ACE, that is, where B in Eq. (2) consists of all storms in a given year. Despite differences in the 1980–2004 linear trends, there is remarkable agreement between the three time series. It is notable that while North Atlantic TC numbers are poorly simulated in CAM4 throughout, and in CAM5 after 1995, simulated global ACE agrees in both magnitude and variability with the IBTrACS estimate. In particular, both models simulate the sudden drop in global ACE between 1997 and 1998 along with the low but slowly rising values between 1998 and 2004 (e.g., Klotzbach 2006; Maue 2011).

The overall agreement in global ACE exists despite large differences in the geographical distribution of ACE (Table 3). While Northern and Southern Hemisphere contributions are similar in CAM4, CAM5, and IBTrACS, contributions from the major basins in the Northern Hemisphere are not. We see, for example, that

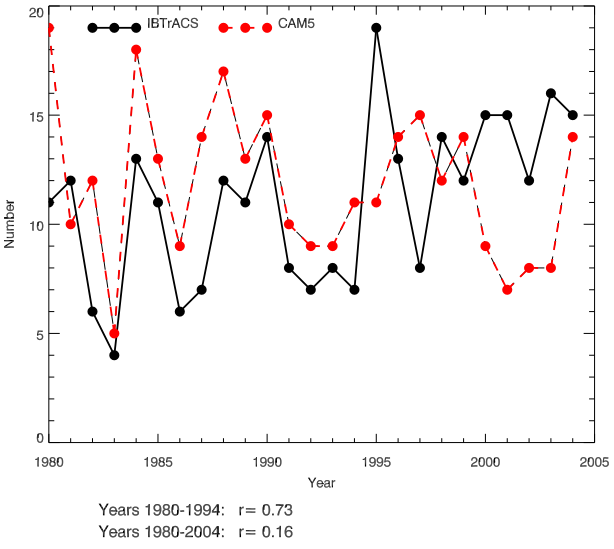

FIG. 17. Tropical cyclone numbers in North Atlantic basin as a function of year for CAM5 0.23 × 0.31 (red) and IBTrACS (black).

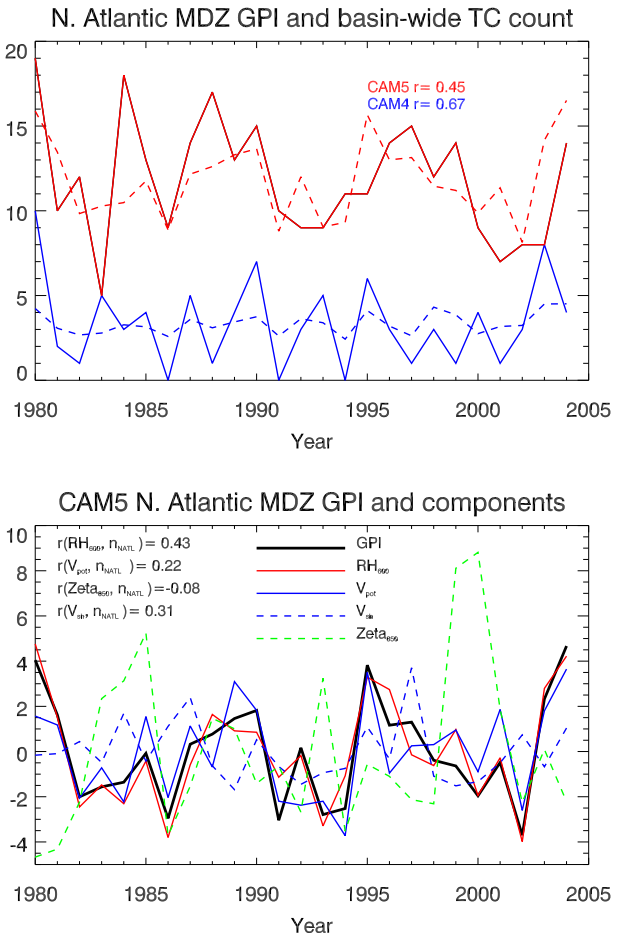

FIG. 18. (top) Tropical cyclone numbers in North Atlantic (solid lines) and area-averaged GPI (see text) (dashed lines) as a function of year for CAM4 0.23 × 0.31 (blue lines) and CAM5 0.23 × 0.31 (red lines). Averages of GPI for each year are for the active North Atlantic season (i.e., June–November). GPI curves for each model have been scaled to equal the corresponding simulated annual mean TC number averaged over 1980–2004. (bottom) CAM5 North Atlantic GPI and its four components as a function of year. GPI (thick black curve) has been scaled as in the top panel. Mean values for 1980–2004 of GPI and all components have been subtracted for easier comparison of time variations. Correlations of the four GPI components with simulated North Atlantic storm numbers are given at the top of the figure.

in CAM4 the North Indian Ocean contributes 10% of the total global ACE while the North Atlantic contributes around 4% compared with 2% and 13% in IBTrACS, respectively. On the other hand, in CAM5 the northwest Pacific contributes 22% while the northeast Pacific contributes 33%, compared with 40% and 17% in IBTrACS and 33% and 22% in CAM4. It is noteworthy that both models and IBTrACS assign around 55% of global ACE to the combined northeast and northwest Pacific, despite differences in how this is partitioned. The correlation of global ACE with combined northeast and northwest Pacific ACE is also high for both CAM4 (0.88) and CAM5 (0.86), as well as for IBTrACS (0.86). This suggests that the high correlations seen in Fig. 19 are driven by total Northern Hemispheric Pacific TC activity, which is well simulated despite discrepancies in the partition between the eastern and western portions of the basin.

8. Summary and discussion

This paper presents an initial comparison of extended AMIP-style experiments using the Community Atmosphere Model versions 4 and 5 (CAM4 and CAM5) at resolutions of 0.9° latitude × 1.25° longitude (0.9 × 1.25) and 0.23° latitude × 0.31° longitude (0.23 × 0.31). The experiments were run from 1 January 1979 through 31 August 2005. A striking result of increasing horizontal resolution, without physics retuning, is a large reduction in cloud radiative forcing (Fig. 1). This happens for both CAM4 and CAM5 although the pattern of change is different in each model, with high-latitude reductions in cloud forcing predominating in CAM4 and tropical reductions predominating in CAM5. Our final AMIP configuration for CAM4 0.23 × 0.31 incorporated a change to the ice cloud parameterization to mitigate the reduction in high-latitude cloud radiative forcing [section 2a(2)]. The final configuration for CAM5 0.23 × 0.31 contains no changes to model physics from those used at 0.9 × 1.25, although prescribed aerosols are used in place of fully prognostic aerosols [section 2a(1)].

The first result of this comparison is that simulated, large-scale, seasonal-mean climatologies do not improve dramatically, even as resolution is increased

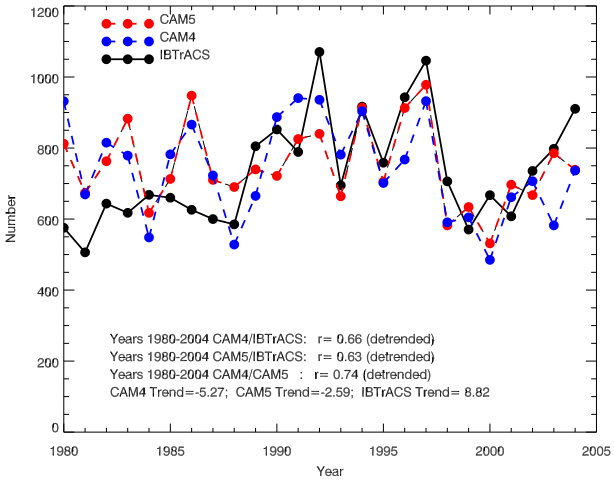

FIG. 19. Annual mean global ACE as a function of year for CAM4 0.23 × 0.31 (blue), CAM5 0.23 × 0.31 (red), and IBTrACS (black). Correlations between the detrended time series are given.

fourfold from 0.9 × 1.25 to 0.23 × 0.31. In some cases, noticeable deterioration takes place, as occurs for the simulated Pacific precipitation patterns in CAM5 (Fig. 8), where the double ITCZ bias is clearly worse at 0.23 × 0.31 than it was at 0.9 × 1.25. Simulation features that do exhibit improvement at high resolution are, not surprisingly, ones that may be related to topographically forced flows. This is especially true for CAM4 where, for example, the simulation of wintertime sea level pressure at high latitudes is visibly improved at 0.23 × 0.31 compared to 0.9 × 1.25 (Fig. 6). Indian summer monsoon precipitation is also improved in CAM4 0.23 × 0.31 (Fig. 7), as is the overall Taylor score for land precipitation and U850 in JJA (Fig. 3). In CAM5 most of these features do not improve as dramatically, and some even degrade slightly as is the case for winter sea level pressure sea level, at high resolution. This may reflect the fact that CAM5 incorporates a parameterization of low-level orographic drag that has been tuned for 0.9 × 1.25 or coarser resolutions (section 4c). This parameterization may not give good results at higher resolutions, leading to muted improvements, or even deterioration, in the simulation of topographic flows at high resolution.

While it is disappointing not to see improvements in large-scale features, an equally important motivation for increasing climate model resolution is to capture important regional and mesoscale circulations. Section 6 examined winter and summer precipitation over the United States. Increasing resolution produces very different responses in these two seasons. Wintertime precipitation over the southeast United States (Fig. 13) shows large increases as resolution increases. This can be traced to enhanced moisture transport from the Gulf of Mexico (Fig. 14). Whether the enhanced moisture transport is primarily a topographic effect or simply a consequence of better resolved midlatitude cyclonic storms is not yet clear.

TABLE 3. Annual-mean global ACE and percentages contributed by different regions or basins in CAM4, CAM5, and IBTrACS for 1980–2004.

Statistic	CAM4	CAM5	IBTrACS
Global ACE (10^{-4} kt^2)	741	750	734
NH (%)	69	74	73
SH (%)	31	26	27
North Atlantic (%)	4	16	13
Northeast Pacific (%)	22	33	17
Northwest Pacific (%)	33	22	40
North Indian Ocean (%)	10	3	2

Summertime precipitation over most of the United States east of the Rocky Mountains is not significantly affected by increased resolution. In particular, the model at 0.23 × 0.31 still fails to simulate the observed nocturnal maximum in precipitation over the Great Plains, which has been attributed to eastward propagating mesoscale convective complexes (MCCs) that originate near the mountains in midafternoon. Hints of such features are in fact seen in large-scale (versus convective) precipitation in the 0.23 × 0.31 simulations where they contribute to nocturnal maxima in large-scale precipitation (Fig. 15). Determining whether MCCs can be accurately resolved at any resolution with CAM's current physical parameterizations is an important question for future research.

Tropical cyclones (TCs) are a critical simulation target for high-resolution climate models. Both CAM4 and CAM5 0.23 × 0.31 explicitly resolve TCs and also accurately capture important aspects of their climatological distribution. Both models simulate reasonable mean track densities compared to IBTrACS estimates, although both also exhibit notable biases (Fig. 16). CAM5 does a credible job of simulating North Atlantic hurricane activity, but it underestimates TC activity in the northwest Pacific. CAM4, on the other hand, does a somewhat better job in reproducing northwest Pacific track densities, but seriously underpredicts North Atlantic activity. An intriguing and baffling result is that both models do an excellent job of reproducing the observed behavior of global accumulated cyclone energy (ACE) despite the large basin-to-basin differences in their TC climatologies. It is likely that the models' mean climate biases contribute to errors in the simulated TC distribution, although the nature of this possible influence is not clear.

It is clear that simply increasing horizontal resolution to the 10-km range will not produce dramatically improved

climate simulations. Existing cloud and convection parameterizations in CAM were developed for resolutions that are coarser by an order of magnitude. Assumptions of scale separation, as well as that of sufficiently large sample size for statistical equilibrium, break down at high resolution (e.g., Jones and Randall 2011). In addition, many existing physical parameterization contain poorly understood dependencies on time step size (e.g., Williamson and Olson 2003) that can also affect their performance as spatial resolution is increased, since physics time steps are also typically reduced at high resolution.

Nevertheless, important mesoscale circulations such as TCs begin to appear with reasonable climatological characteristics in high-resolution climate simulations. Some regional precipitation features are arguably better, and precipitation intensity distributions also improve at high resolution (Fig. 10). These facts point to an important role for high-resolution climate simulations in assessing the societal impacts of weather and climate. Development of physics parameterizations that perform well near 10-km horizontal resolution, allowing models to capture both long-term means and high-frequency variability, is an urgent need.

Acknowledgments. Partial support for this work was provided through the Scientific Discovery through Advanced Computing (SciDAC) program funded by U.S. Department of Energy, Office of Science, Advanced Scientific Computing Research. This research used computing resources of the Oak Ridge Leadership Computing Facility and of the National Energy Research Scientific Computing Center, which are supported by the Office of Science of the Department of Energy. We would also like to thank David Williamson for useful discussions, and three anonymous reviewers for helpful questions and comments on the manuscript.

APPENDIX

Simple Tracking of Tropical Cyclones

Our 25-yr CAM4 0.23 × 0.31 run saved only limited variables at high time resolution. Instantaneous winds at the lowest model level were saved every 3 h along with precipitation and surface pressure. To perform tropical cyclone tracking in a consistent manner in the CAM4 and CAM5 we devised a simple tracking scheme that relies on winds and surface pressure alone. The first step is to calculate deviations in instantaneous 3-hourly surface pressure from a 14-day retrospective mean $p^*_{\rm sfc} = p_{\rm sfc} - [p_{\rm sfc}]_{(-14{\rm d},0)}$. Fields of $p^*_{\rm sfc}$ are then searched for local minima, and if the depth of a minimum exceeds 3 hPa, a candidate low is assigned. Next, near-surface wind speed is examined in an area within 50 km of the candidate low. If a maximum wind of more than 10 m s^{-1} is found the low is kept for tracking.

Tracking of the lows over 3-h intervals is relatively straightforward. We begin potential tracks with the candidate lows identified above. For the second element in any particular track we simply choose the low at t + 3 h nearest to the original low at t. If another low is not located within a 200-km search radius, the track is not continued. In subsequent time steps the motion of the low between $t - 3$ h and t is extrapolated over the next 3 h. The next track element at $t + 3$ h is then chosen to be the low closest to the extrapolated location. If another low is not located within a 200-km search radius, the track is terminated. Values of instantaneous relative vorticity along each track are recorded for later use.

Without any further filtering the scheme at this point provides a ''generous'' categorization of disturbances as tropical cyclones, that is, many disturbances are retained that would be discarded after closer scrutiny. In addition, the simple scheme occasionally breaks up tracks in the early phases of developing TCs if $p^*_{\rm sfc}$ remains close to the threshold value for an extended time. This can lead to multiple counting of a single storm. Nevertheless, the simple scheme gives results surprisingly close to those obtained with the GFDL tracking algorithm (Vitart et al. 1997; Zhao et al. 2009), which is a more sophisticated algorithm employing multiple levels of temperature data. Table A1 compares results obtained with this simple scheme ALG0 and the GFDL tracking algorithm. The two schemes give similar numbers for global ACE and the correlation of the yearly hurricane count between the schemes is high (0.83). Statistics that are less satisfactory in ALG0 are those that rely on counting weak disturbances, such as the global average number of storms per year. Correlation of North Atlantic TC numbers with GFDL's is modest (0.42) but still significant at the 95% level. Note that global ACE is high for both ALG0 and GFDL schemes compared to IBTrACS.

The ALG0 scheme produces high global ACE compared to IBTrACS, as well as high TC numbers compared to both IBTrACS and the GFDL tracking scheme. Two modifications are introduced to alleviate these problems. First, the lowest-level model winds represent a level around 60 m rather than 10 m, which is the level used in the IBTrACS data, so we scale model winds using the wind power law

$$u_{10{\rm m}} = \left(\frac{10}{60}\right)^{\alpha} u_{60{\rm m}}, \qquad \text{(A1)}$$

TABLE A1. Tropical cyclone statistics obtained from various tracking algorithms applied to CAM5 0.23 × 0.31 fields compared with results from IBTrACS. TC and hurricane numbers and global ACE for ALG0, ALG1, and IBTrACS are for years 1980–2004. Statistics for GFDL as well as correlations with GFDL are for 1982–2000.

Statistic	GFDL	ALG0	ALG1	IBTrACS
Global TCs per year	84	186	90	84
Global hurricanes per year	51	68	41	39
Correlation of North Atlantic TC no. with GFDL	—	0.42	0.67	0.24
Correlation of North Atlantic hurricane no. with GFDL	—	0.83	0.88	−0.03
Global ACE (10^{-4} kt^2)	1118	1295	750	734

where the exponent α is chosen to be 0.11, a value appropriate over ocean (Hsu et al. 1994). Second, we impose a threshold value 0.0013 s^{-1} for low-level vorticity magnitude $|\zeta_{60m}|$ along each track. Tracks for which $|\zeta_{60m}|$ never exceeds this value are eliminated. This eliminates many low-latitude tracks that are associated with intense precipitation and low pressure but do not develop appreciable circulation. The threshold value is chosen to yield a global average of around 90 storms per year.

With these additional conditions the tracking scheme ALG1 produces results comparable in most respects to those from the GFDL tracking scheme. The global TC number in ALG1 is slightly higher but comparable to that in GFDL, 90 versus 84. The correlation of North Atlantic TC numbers in ALG1 with GFDL's is high (0.67). The discrepancy between GFDL global ACE values and those in ALG1 and IBTrACS is attributable to the wind scaling in Eq. (A1). When this scaling is applied to wind speeds in the GFDL tracks, global annual-average ACE becomes 752 × 10^{-4} kt^2, comparable to that in ALG1 and IBTrACS.

REFERENCES

Bacmeister, J. T., M. J. Suarez, and F. R. Robertson, 2006: Rain reevaporation, boundary layer–convection interactions, and Pacific rainfall patterns in an AGCM. *J. Atmos. Sci.,* **63,** 3383–3403, doi:10.1175/JAS3791.1.

——, P. H. Lauritzen, A. Dai, and J. E. Truesdale, 2012: Assessing possible dynamical effects of condensate in high-resolution climate simulations. *Geophys. Res. Lett.,* **39,** L04806, doi:10.1029/2011GL050533.

Bell, G. D., and M. Chelliah, 2006: Leading tropical modes associated with interannual and multidecadal fluctuations in North Atlantic hurricane activity. *J. Climate,* **19,** 590–612, doi:10.1175/JCLI3659.1.

——, and Coauthors, 2000: Climate assessment for 1999. *Bull. Amer. Meteor. Soc.,* **81,** S1–S50, doi:10.1175/1520-0477(2000)81[s1:CAF]2.0.CO;2.

Bister, M., and K. A. Emanuel, 2002: Low frequency variability of tropical cyclone potential intensity. 1. Interannual to interdecadal variability. *J. Geophys. Res.,* **107,** 4801, doi:10.1029/2001JD000776 .

Boyle, J., and S. Klein, 2010: Impact of horizontal resolution on climate model forecasts of tropical precipitation and diabatic heating for the TWP-ICE period. *J. Geophys. Res.,* **115,** D23113, doi:10.1029/2010JD014262.

Camargo, S. J., and A. H. Sobel, 2005: Western North Pacific tropical cyclone intensity and ENSO. *J. Climate,* **18,** 2996–3006, doi:10.1175/JCLI3457.1.

——, K. A. Emanuel, and A. H. Sobel, 2007: Use of a genesis potential index to diagnose ENSO effects on tropical cyclone genesis. *J. Climate,* **20,** 4819–4834, doi:10.1175/JCLI4282.1.

Carbone, R., J. Tuttle, D. Ahijevych, and S. Trier, 2002: Inferences of predictability associated with warm season precipitation episodes. *J. Atmos. Sci.,* **59,** 2033–2056, doi:10.1175/1520-0469(2002)059<2033:IOPAWW>2.0.CO;2.

Dai, A., 2006: Precipitation characteristics in eighteen coupled climate models. *J. Climate,* **19,** 4605–4630, doi:10.1175/JCLI3884.1.

Dee, D., and Coauthors, 2011: The ERA-Interim reanalysis: Configuration and performance of the data assimilation system. *Quart. J. Roy. Meteor. Soc.,* **137,** 553–597, doi:10.1002/qj.828.

Dennis, J., and Coauthors, 2012: CAM-SE: A scalable spectral element dynamical core for the Community Atmosphere Model. *Int. J. High Perform. Comput. Appl.,* **26,** 74–89, doi:10.1177/1094342011428142.

Dunion, J. P., and C. S. Velden, 2004: The impact of the Saharan air layer on Atlantic tropical cyclone activity. *Bull. Amer. Meteor. Soc.,* **85,** 353–365, doi:10.1175/BAMS-85-3-353.

Easter, R. C., and Coauthors, 2004: MIRAGE: Model description and evaluation of aerosols and trace gases. *J. Geophys. Res.,* **109,** D20210, doi:10.1029/2004JD004571.

Emanuel, K. A., and D. Nolan, 2004: Tropical cyclone activity and the global climate system. *Preprints, 26th Conf. on Hurricanes and Tropical Meteorology,* Miami, FL, Amer. Meteor. Soc., 10A.2. [Available online at https://ams.confex.com/ams/26HURR/techprogram/paper_75463.htm.]

Gettelman, A., and Coauthors, 2010: Global simulations of ice nucleation and ice supersaturation with an improved cloud scheme in the Community Atmosphere Model. *J. Geophys. Res.,* **115,** D18216, doi:10.1029/2009JD013797.

Ghan, S. J., and R. C. Easter, 2006: Impact of cloud-borne aerosol representation on aerosol direct and indirect effects. *Atmos. Chem. Phys.,* **6**, 4163–4174, doi:10.5194/acp-6-4163-2006.

Goldenberg, S. B., C. W. Landsea, A. M. Mestas-Nuñez, and W. M. Gray, 2001: The recent increase in Atlantic hurricane activity: Causes and implications. *Science,* **293,** 474–479, doi:10.1126/science.1060040.

Harper, B., J. Kepert, and J. Ginger, 2010: Guidelines for converting between various wind averaging periods in tropical cyclone conditions. TCP Sub-Project Rep. WMO/TD 1555, 64 pp. [Available online at http://www.wmo.int/pages/prog/www/tcp/documents/WMO_TD_1555_en.pdf.]

Hsu, S., E. Meindl, and D. Gilhousen, 1994: Determining the power-law wind-profile exponent under near-neutral stability conditions at sea. *J. Appl. Meteor.,* **33,** 757–765, doi:10.1175/1520-0450(1994)033<0757:DTPLWP>2.0.CO;2.

Huffman, G., and Coauthors, 1997: The Global Precipitation Climatology Project (GPCP) combined precipitation dataset. *Bull. Amer. Meteor. Soc.,* **78,** 5–20, doi:10.1175/1520-0477(1997)078<0005:TGPCPG>2.0.CO;2.

——, and Coauthors, 2007: The TRMM Multisatellite Precipitation Analysis (TMPA): Quasi-global, multiyear, combined-sensor precipitation estimates at fine scales. *J. Hydrometeor.,* **8,** 38–55, doi:10.1175/JHM560.1.

Hurrell, J. W., J. J. Hack, D. Shea, J. M. Caron, and J. Rosinski, 2008: A new sea surface temperature and sea ice boundary dataset for the Community Atmosphere Model. *J. Climate,* **21,** 5145–5153, doi:10.1175/2008JCLI2292.1.

Jones, T. R., and D. A. Randall, 2011: Quantifying the limits of convective parameterizations. *J. Geophys. Res.,* **116,** D08210, doi:10.1029/2010JD014913.

Jung, T., and Coauthors, 2012: High-resolution global climate simulations with the ECMWF model in Project Athena: Experimental design, model climate, and seasonal forecast skill. *J. Climate,* **25,** 3155–3172, doi:10.1175/JCLI-D-11-00265.1.

Kiehl, J. T., T. L. Schneider, P. J. Rasch, and M. C. Barth, 2000: Radiative forcing due to sulfate aerosols from simulations with the National Center for Atmospheric Research Community Climate Model, version 3. *J. Geophys. Res.,* **105,** 1441–1457, doi:10.1029/1999JD900495.

Kirtman, B. P., and Coauthors, 2013: Impact of ocean model resolution on CCSM climate simulations. *Climate Dyn.,* **39,** 1303–1328, doi:10.1007/s00382-012-1500-3.

Klotzbach, P. J., 2006: Trends in global tropical cyclone activity over the past twenty years (1986–2005). *Geophys. Res. Lett.,* **33,** L10805, doi:10.1029/2006GL025881.

——, and W. M. Gray, 2008: Multidecadal variability in North Atlantic tropical cyclone activity. *J. Climate,* **21,** 3929–3935, doi:10.1175/2008JCLI2162.1.

Knapp, K., M. Kruk, D. Levinson, H. Diamond, and C. Neumann, 2010: The international best track archive for climate stewardship (IBTrACS): Unifying tropical cyclone data. *Bull. Amer. Meteor. Soc.,* **91,** 363–376, doi:10.1175/2009BAMS2755.1.

Kristjánsson, J., J. Edwards, and D. Mitchell, 2000: Impact of a new scheme for optical properties of ice crystals on climates of two GCMs. *J. Geophys. Res.,* **105,** 10 063–10 079, doi:10.1029/2000JD900015.

Lauritzen, P. H., J. Bacmeister, M. A. Taylor, and R. B. Neale, 2012a: New topography software for CAM. *Proc. NCAR Atmosphere Model Working Group Meeting,* Boulder, CO, NCAR. [Available online at http://www.cesm.ucar.edu/working_groups/Atmosphere/Presentations/2012/lauritzen.pdf.]

——, A. A. Mirin, J. Truesdale, K. Raeder, J. L. Anderson, J. Bacmeister, and R. B. Neale, 2012b: Implementation of new diffusion/filtering operators in the CAM-FV dynamical core. *Int. J. High Perform. Comput. Appl.,* **26,** 63–73, doi:10.1177/1094342011410088.

Lin, J.-L., and Coauthors, 2006: Tropical intraseasonal variability in 14 IPCC AR4 climate models. Part I: Convective signals. *J. Climate,* **19,** 2665–2690, doi:10.1175/JCLI3735.1.

Lin, S.-J., 2004: A ''vertically Lagrangian'' finite-volume dynamical core for global models. *Mon. Wea. Rev.,* **132,** 2293–2307, doi:10.1175/1520-0493(2004)132<2293:AVLFDC>2.0.CO;2.

Loeb, N., B. Wielicki, D. Doelling, G. Smith, D. Keyes, S. Kato, N. Manalo-Smith, and T. Wong, 2009: Toward optimal closure of the earth's top-of-atmosphere radiation budget. *J. Climate,* **22,** 748–766, doi:10.1175/2008JCLI2637.1.

Maddox, R., 1980: Mesoscale convective complexes. *Bull. Amer. Meteor. Soc.,* **61,** 1374–1387, doi:10.1175/1520-0477(1980)061<1374:MCC>2.0.CO;2.

Manganello, J. V., and Coauthors, 2012: Tropical cyclone climatology in a 10-km global atmospheric GCM: Toward weather-resolving climate modeling. *J. Climate,* **25,** 3867–3893, doi:10.1175/JCLI-D-11-00346.1.

Maue, R., 2011: Recent historically low global tropical cyclone activity. *Geophys. Res. Lett.,* **38,** L14803, doi:10.1029/2011GL047711.

Menkes, C., M. Lengaigne, P. Marchesiello, N. Jourdain, E. Vincent, J. Lefèvre, F. Chauvin, and J. Royer, 2012: Comparison of tropical cyclogenesis indices on seasonal to interannual timescales. *Climate Dyn.,* **38,** 301–321, doi:10.1007/s00382-011-1126-x.

Morrison, H., and A. Gettelman, 2008: A new two-moment bulk stratiform cloud microphysics scheme in the Community Atmosphere Model, version 3 (CAM3). Part I: Description and numerical tests. *J. Climate,* **21,** 3642–3659, doi:10.1175/2008JCLI2105.1.

Neale, R., J. Richter, and M. Jochum, 2008: The impact of convection on ENSO: From a delayed oscillator to a series of events. *J. Climate,* **21,** 5904–5924, doi:10.1175/2008JCLI2244.1.

——, and Coauthors, 2010: Description of the NCAR Community Atmosphere Model (CAM 4.0). NCAR Tech. Note NCAR-TN-485+STR, 212 pp.

——, and Coauthors, 2012: Description of the NCAR Community Atmosphere Model (CAM 5.0). NCAR Tech. Note NCAR-TN-486+STR, 274 pp.

Putman, W. M., S.-J. Lin, and B.-W. Shen, 2005: Cross-platform performance of a portable communication module and the NASA finite volume general circulation model. *Int. J. High Perform. Comput. Appl.,* **19,** 213–223, doi:10.1177/1094342005056101.

Randel, D., T. Greenwald, T. Vonder Haar, G. Stephens, M. Ringerud, and C. Combs, 1996: A new global water vapor dataset. *Bull. Amer. Meteor. Soc.,* **77,** 1233–1246, doi:10.1175/1520-0477(1996)077<1233:ANGWVD>2.0.CO;2.

Rasch, P. J., and J. E. Kristjansson, 1998: A comparison of CCM3 model climate using diagnosed and predicted condensate parameterizations. *J. Climate,* **11,** 1587–1614, doi:10.1175/1520-0442(1998)011<1587:ACOTCM>2.0.CO;2.

Richter, J. H., F. Sassi, and R. R. Garcia, 2010: Toward a physically based gravity wave source parameterization in a general circulation model. *J. Atmos. Sci.,* **67,** 136–156, doi:10.1175/2009JAS3112.1.

Roundy, P. E., 2012: The spectrum of convectively coupled Kelvin waves and the Madden–Julian oscillation in regions of low-level easterly and westerly background flow. *J. Atmos. Sci.,* **69,** 2107–2111, doi:10.1175/JAS-D-12-060.1.

Satoh, M., T. Matsuno, H. Tomita, H. Miura, T. Nasuno, and S. Iga, 2008: Nonhydrostatic icosahedral atmospheric model (NICAM) for global cloud resolving simulations. *J. Comput. Phys.,* **227,** 3486–3514, doi:10.1016/j.jcp.2007.02.006.

Stephens, G., and Coauthors, 2010: Dreary state of precipitation in global models. *J. Geophys. Res.,* **115,** D24211, doi:10.1029/2010JD014532.

Storelvmo, T., J. E. Kristjánsson, and U. Lohmann, 2008: Aerosol influence on mixed-phase clouds in CAM-Oslo. *J. Atmos. Sci.,* **65,** 3214–3230, doi:10.1175/2008JAS2430.1.

Taylor, K., 2001: Summarizing multiple aspects of model performance in a single diagram. *J. Geophys. Res.,* **106,** 7183–7192, doi:10.1029/2000JD900719.

——, D. Williamson, and F. Zwiers, 2000: The sea surface temperature and sea-ice concentration boundary conditions for AMIP II simulations. PCMDI Rep. 60, 25 pp. [Available online at http://www-pcmdi.llnl.gov/publications/ab60.html.]

Trier, S., C. Davis, D. Ahijevych, M. Weisman, and G. Bryan, 2006: Mechanisms supporting long-lived episodes of propagating nocturnal convection within a 7-day WRF model simulation. *J. Atmos. Sci.,* **63,** 2437–2461, doi:10.1175/JAS3768.1.

Turner, D. D., 2005: Arctic mixed-phase cloud properties from AERI lidar observations: Algorithm and results from SHEBA. *J. Appl. Meteor.,* **44,** 427–444, doi:10.1175/JAM2208.1.

Tuttle, J., and C. Davis, 2006: Corridors of warm season precipitation in the central United States. *Mon. Wea. Rev.,* **134,** 2297–2317, doi:10.1175/MWR3188.1.

Vitart, F., J. Anderson, and W. Stern, 1997: Simulation of interannual variability of tropical storm frequency in an ensemble of GCM integrations. *J. Climate,* **10,** 745–760, doi:10.1175/1520-0442(1997)010<0745:SOIVOT>2.0.CO;2.

Williamson, D. L., and J. G. Olson, 2003: Dependence of aqua-planet simulations on time step. *Quart. J. Roy. Meteor. Soc.,* **129,** 2049–2064, doi:10.1256/qj.02.62.

Xie, P., J. Janowiak, P. Arkin, R. Adler, A. Gruber, R. Ferraro, G. Huffman, and S. Curtis, 2003: GPCP pentad precipitation analyses: An experimental dataset based on gauge observations and satellite estimates. *J. Climate,* **16,** 2197–2214, doi:10.1175/2769.1.

Zhang, G., and N. McFarlane, 1995: Sensitivity of climate simulations to the parameterization of cumulus convection in the Canadian Climate Centre general circulation model. *Atmos.–Ocean,* **33,** 407–446, doi:10.1080/07055900.1995.9649539.

Zhao, M., I. M. Held, S.-J. Lin, and G. A. Vecchi, 2009: Simulations of global hurricane climatology, interannual variability, and response to global warming using a 50-km resolution GCM. *J. Climate,* **22,** 6653–6678, doi:10.1175/2009JCLI3049.1.